CHAPTER

9

Boundary Layers and Related Topics

CHAPTER OBJECTIVES

- To describe the boundary-layer concept and the mathematical simplifications it allows in the complete equations of motion for a viscous fluid.

- To present the equations of fluid motion for attached laminar boundary layers.

- To provide a variety of exact and approximate steady laminar boundary-layer solutions.

- To describe the basic phenomenology of boundary-layer transition and separation.

- To discuss the Reynolds number dependent phenomena associated with flow past bluff bodies.

- To illustrate the use of a boundary-layer solution methodology for free and wall-bounded jet flows.

9.1. INTRODUCTION

Until the beginning of the twentieth century, analytical solutions of steady fluid flows were generally known for two typical situations. One of these was that of parallel viscous flows and low Reynolds number flows, in which the nonlinear advective terms were zero and the balance of forces was that between pressure and viscous forces. The second type of solution was that of inviscid flows around bodies of various shapes, in which the balance of forces was that between inertia and pressure forces. Although the equations of motion are nonlinear in this second situation, the velocity field can be determined by solving the linear Laplace equation. These irrotational solutions predicted pressure forces on a streamlined body that agreed surprisingly well with experimental data for flow of fluids of small viscosity. However, these solutions also predicted zero drag force and a nonzero tangential velocity at the body surface, features that did not agree with the experiments.

In 1905 Ludwig Prandtl, an engineer by profession and therefore motivated to find realistic fields near bodies of various shapes, first hypothesized that, for small viscosity, the viscous forces are negligible everywhere except close to solid boundaries where the no-slip condition has to be satisfied. The thickness of these boundary layers approaches zero as the viscosity goes to zero. Prandtl's hypothesis reconciled two rather contradictory facts. It supported the intuitive idea that the effects of viscosity are indeed negligible in most of the flow field if ν is small, but it also accounted for drag by insisting that the no-slip condition must be satisfied at a solid surface, no matter how small the viscosity. This reconciliation was Prandtl's aim, which he achieved brilliantly, and in such a simple way that it now seems strange that nobody before him thought of it. Prandtl also showed how the equations of motion within the boundary layer can be simplified. Since the time of Prandtl, the concept of the boundary layer has been generalized, and the mathematical techniques involved have been formalized, extended, and applied in other branches of physical science (see van Dyke, 1975; Bender & Orszag, 1978; Kevorkian & Cole 1981; Nayfeh, 1981). The concept of the boundary layer is considered a cornerstone in the intellectual foundation of fluid mechanics.

This chapter presents the boundary-layer hypothesis and examines its consequences. The equations of fluid motion within the boundary layer can be simplified because of the layer's thinness, and exact or approximate solutions can be obtained in many cases. In addition, boundary-layer phenomena provide explanations for the lift and drag characteristics of bodies of various shapes in high Reynolds number flows, including turbulent flows. In particular, the fluid mechanics of curved sports-ball trajectories is described here.

The fundamental assumption of boundary-layer theory is that the layer is thin compared to other length scales such as the length of the surface or its local radius of curvature. Across this thin layer, which can exist only in high Reynolds number flows, the velocity varies rapidly enough for viscous effects to be important. This is shown in Figure 9.1, where the boundary-layer thickness is greatly exaggerated. (On a typical airplane wing, which may have a chord of several meters, the boundary-layer thickness is of order one centimeter.) However, thin viscous layers exist not only next to solid walls but also in the form of jets, wakes, and shear layers if the Reynolds number is sufficiently high. So, to be specific, we shall first consider the boundary layer contiguous to a solid surface, adopting a curvilinear

FIGURE 9.1 A boundary layer forms when a viscous fluid moves over a solid surface. Only the boundary layer on the top surface of the foil is depicted in the figure and its thickness, δ, is greatly exaggerated. Here, U_∞ is the oncoming free-stream velocity and U_e is the velocity at the edge of the boundary layer. The usual boundary-layer coordinate system allows the x-axis to coincide with a mildly curved surface so that the y-axis always lies in the surface-normal direction.
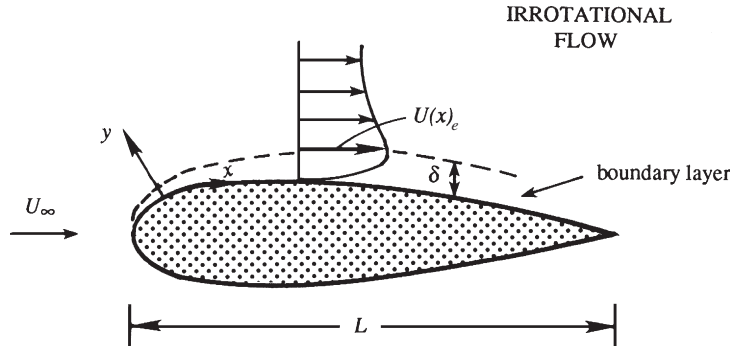
coordinate system that conforms to the surface where x increases along the surface and y increases normal to it. Here the surface may be curved but the radius of curvature of the surface must be much larger than the boundary-layer thickness. We shall refer to the solution of the irrotational flow outside the boundary layer as the *outer* problem and that of the boundary-layer flow as the *inner* problem.

For a thin boundary layer that is contiguous to the solid surface on which it has formed, the full equations of motion for a constant-density constant-viscosity fluid, (4.10) and (8.1), may be simplified. Let $\overline{\delta}(x)$ be the average thickness of the boundary layer at downstream location x on the surface of a body having a local radius of curvature R. The steady-flow momentum equation for the surface-parallel velocity component, u, is

$$u\frac{\partial u}{\partial x} + v\frac{\partial u}{\partial y} = -\frac{1}{\rho}\frac{\partial p}{\partial x} + \nu\left(\frac{\partial^2 u}{\partial x^2} + \frac{\partial^2 u}{\partial y^2}\right), \tag{9.1}$$

which is valid when $\overline{\delta}/R \ll 1$. The more general curvilinear form for arbitrary $R(x)$ is given in Goldstein (1938) and Schlichting (1979), but the essential features of viscous boundary layers can be illustrated via (9.1) without additional complications.

Let a characteristic magnitude of u be U_∞, the velocity at a large distance upstream of the body, and let L be the stream-wise distance over which u changes appreciably. The longitudinal length of the body can serve as L, because u within the boundary layer does change in the stream-wise direction by a large fraction of U_∞ over a distance L (Figure 9.2). A measure of $\partial u/\partial x$ is therefore U_∞/L, so that the approximate size of the first advective term in (9.1) is

$$u(\partial u/\partial x) \sim U_\infty^2/L, \tag{9.2}$$

where $\sim$ is to be interpreted as "of order." We shall see shortly that the other advective term in (9.1) is of the same order. The approximate size of the viscous term in (9.1) is

$$\nu(\partial^2 u/\partial y^2) \sim \nu U_\infty/\overline{\delta}^2. \tag{9.3}$$
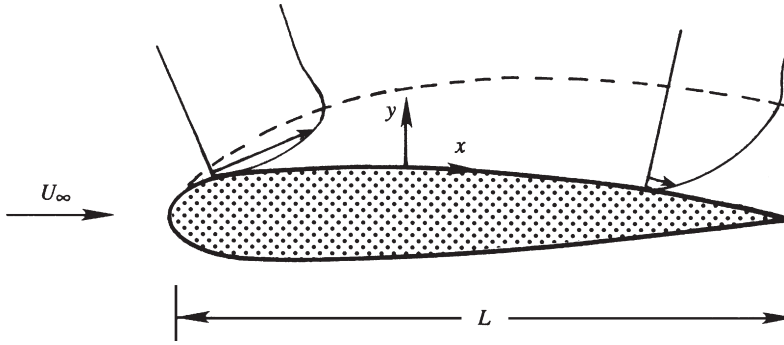
FIGURE 9.2 Velocity profiles at two positions within the boundary layer. Here again, the boundary-layer thickness is greatly exaggerated. The two velocity vectors are drawn at the same distance y from the surface, showing that the variation of u over a distance $x \sim L$ is of the order of the free-stream velocity U_∞.

The magnitude of $\overline{\delta}$ can now be estimated by noting that the advective and viscous terms should be of the same order within the boundary layer. Equating advective and viscous terms in (9.2) and (9.3) leads to:

$$\overline{\delta} \sim \sqrt{\nu L/U_\infty} \quad \text{or} \quad \overline{\delta}/L \sim 1/\sqrt{\text{Re}}. \tag{9.4}$$

This estimate of $\overline{\delta}$ can also be obtained by noting that viscous effects diffuse to a distance of order $[\nu t]^{1/2}$ in time t and that the time-of-flight for a fluid element along a body of length L is of order L/U_∞. Substituting L/U_∞ for t in $[\nu t]^{1/2}$ suggests the viscous layer's diffusive thickness at $x = L$ is of order $[\nu L/U_\infty]^{1/2}$.

A formal simplification of the equations of motion within the boundary layer can now be performed. The basic idea is that variations across the boundary layer occur over a much shorter length scale than variations along the layer, that is:

$$\partial/\partial x \sim 1/L \quad \text{and} \quad \partial/\partial y \sim 1/\overline{\delta}, \tag{9.5}$$

where $\overline{\delta} \ll L$ when $\text{Re} \gg 1$ from (9.4). When applied to the continuity equation, $\partial u/\partial x + \partial v/\partial y = 0$, this derivative scaling requires $U_\infty/L \sim v/\overline{\delta}$, so the proper velocity scale for v is $\overline{\delta}U_\infty/L = U_\infty \text{Re}^{-1/2}$. At high Re, experimental data show that the pressure distribution on the body is nearly that in an irrotational flow around the body, implying that the pressure variations scale with the fluid inertia: $p - p_\infty \sim \rho U_\infty^2$. Thus, the proper dimensionless variables for boundary-layer flow are:

$$x^* = x/L, \; y^* = y/\overline{\delta} = (y/L)\text{Re}^{1/2}, \; u^* = u/U_\infty, \; v^* = (v/U_\infty)\text{Re}^{1/2}, \; \text{and} \; p^* = (p - p_\infty)/\rho U_\infty^2. \tag{9.6}$$

For the coordinates and the velocities, this scaling is similar to that of (8.14) with $\varepsilon = \text{Re}^{-1/2}$. The primary effect of (9.6) is a magnification of the surface-normal coordinate y and velocity v by a factor of $\text{Re}^{1/2}$ compared to the stream-wise coordinate x and velocity u. In terms of these dimensionless variables, the steady two-dimensional equations of motion are:

$$\frac{\partial u^*}{\partial x^*} + \frac{\partial v^*}{\partial y^*} = 0, \tag{8.15}$$

$$u^* \frac{\partial u^*}{\partial x^*} + v^* \frac{\partial u^*}{\partial y^*} = -\frac{\partial p^*}{\partial x^*} + \frac{1}{Re} \frac{\partial^2 u^*}{\partial x^*} + \frac{\partial^2 u^*}{\partial y^*}, \text{ and} \tag{9.7}$$

$$\frac{1}{Re}\left(u^* \frac{\partial v^*}{\partial x^*} + v^* \frac{\partial v^*}{\partial y^*}\right) = -\frac{\partial p^*}{\partial y^*} + \frac{1}{Re^2} \frac{\partial^2 v^*}{\partial x^{*2}} + \frac{1}{Re} \frac{\partial^2 v^*}{\partial y^{*2}}, \tag{9.8}$$

where $Re \equiv U_\infty L/\nu$ is an overall Reynolds number. In these equations, each of the dimensionless variables and their derivatives should be of order unity when the scaling assumptions embodied in (9.6) are valid. Thus, it follows that the importance of each term in (8.15), (9.7), and (9.8) is determined by its coefficient. So, as $Re \rightarrow \infty$, the terms with coefficients of $1/Re$ or $1/Re^2$ drop out asymptotically. Thus, the relevant equations for laminar boundary-layer flow, in dimensional form, are:

$$\frac{\partial u}{\partial x} + \frac{\partial v}{\partial y} = 0, \tag{6.2}$$

$$u \frac{\partial u}{\partial x} + v \frac{\partial u}{\partial y} = -\frac{1}{\rho} \frac{\partial p}{\partial x} + \nu \frac{\partial^2 u}{\partial y^2}, \quad \text{and} \quad 0 = -\frac{\partial p}{\partial y}. \tag{9.9, 9.10}$$

This scaling exercise has shown which terms must be kept and which terms may be dropped under the boundary-layer assumption. It differs from the scalings that produced (4.101) and (8.42) because the x and y directions are scaled differently in (9.6) which causes a second derivative term to be retained in (9.9).

Equation (9.10) implies that the pressure is approximately uniform across the boundary layer, an important result. The pressure at the surface is therefore equal to that at the edge of the boundary layer, so it can be found from an ideal outer-flow solution for flow above the surface. Thus, the outer flow imposes the pressure on the boundary layer. This justifies the experimental fact that the observed surface pressures underneath attached boundary layers are approximately equal to that calculated from ideal flow theory. A vanishing $\partial p/\partial y$, however, is not valid if the boundary layer separates from the surface or if the radius of curvature of the surface is not large compared with the boundary-layer thickness.

Although the steady boundary-layer equations (6.2), (9.9), and (9.10) do represent a significant simplification of the full equations, they are still nonlinear second-order partial differential equations that can only be solved when appropriate boundary and matching conditions are specified. If the exterior flow is presumed to be known and irrotational (and the fluid density is constant), the pressure gradient at the edge of the boundary layer can be found by differentiating the steady constant-density Bernoulli equation (without the body force term), $p + \frac{1}{2}\rho U_e^2 = const.$, to find:

$$-\frac{1}{\rho} \frac{dp}{dx} = U_e \frac{dU_e}{dx}, \tag{9.11}$$

where $U_e(x)$ is the velocity at the *edge* of the boundary layer. Equation (9.11) represents a matching condition between the outer solution and the inner boundary-layer solution in the region where both solutions must be valid. The (usual) remaining boundary conditions on the fluid velocities of the inner solution are:

$$u(x, 0) = 0 \quad \text{(no slip at the wall)}, \tag{9.12}$$

$$v(x, 0) = 0 \quad \text{(no flow through the wall)}, \tag{9.13}$$

$$u(x, y \rightarrow \infty) = U_e(x) \quad \text{(matching of inner and outer solutions), and} \tag{9.14}$$

$$u(x_0, y) = u_{in}(y) \quad \text{(inlet boundary condition at } x_0). \tag{9.15}$$

For two-dimensional flow, (6.2), (9.9), and the conditions (9.11) through (9.15), completely specify the inner solution as long as the boundary layer remains thin and contiguous to the surface on which it develops. Condition (9.14) merely means that the boundary layer must join smoothly with the outer flow; for the inner solution, points outside the boundary layer are represented by $y \rightarrow \infty$, although we mean this strictly in terms of the dimensionless distance $y/\overline{\delta} = (y/L)\text{Re}^{1/2} \rightarrow \infty$. Condition (9.15) implies that an initial velocity profile $u_{in}(y)$ at some location x_0 is required for solving the problem. Such a condition is needed because the terms $u \partial u/\partial x$ and $v \partial^2 u/\partial y^2$ give the boundary-layer equations a parabolic character, with x playing the role of a time-like variable. Recall the Stokes problem of a suddenly accelerated plate, discussed in the preceding chapter, where the simplified field equation is $\partial u/\partial t = v \partial^2 u/\partial y^2$. In such problems governed by parabolic equations, the field at a certain time or place depends only on its *past* or *upstream history*. Boundary layers therefore transfer viscous effects only in the *downstream* direction. In contrast, the complete Navier-Stokes equations are elliptic and thus require boundary conditions on the velocity (or its derivative normal to the boundary) upstream, downstream, and on the top and bottom boundaries, that is, all around. (The upstream influence of the downstream boundary condition is a common concern in fluid dynamic computations.)

Considering two dimensions, an ideal outer flow solution from (6.5) or (6.12) and (6.18), and a viscous inner flow solution as described here would seem to fully solve the problem of uniform flow of a viscous fluid past a solid object. The solution procedure could be a two-step process. First, the outer flow is determined from (6.5) or (6.12) and (6.18), neglecting the existence of the boundary layer, an error that gets smaller when the boundary layer becomes thinner. Then, (9.11) could be used to determine the surface pressure, and (6.2) and (9.9) could be solved for the boundary-layer flow using the surface-pressure gradient determined from the outer flow solution. If necessary this process might even be iterated to achieve higher accuracy by re-solving for the outer flow with the first-pass-solution boundary-layer characteristics included, and then proceeding to a second solution of the boundary-layer equations using the corrected outer-flow solution. In practice, such an approach can be successful and it converges when the boundary layer stays thin and attached. However, it does not converge when the boundary layer thickens or departs (separates) from the surface on which it has developed. Boundary-layer separation occurs when the surface shear stress, τ_0, produced by the boundary layer vanishes and reverse (or upstream-directed) flow occurs near the surface. Boundary-layer separation is discussed further in Sections 9.6 and 9.7. Here it is sufficient to point out that ideal flow around nonslender or *bluff* bodies typically produces surface pressure gradients that lead to boundary-layer separation.

In summary, the simplifications of the boundary-layer assumption are as follows. First, diffusion in the stream-wise direction is negligible compared to that in the wall normal direction. Second, the pressure field can be found from the outer flow, so that it is regarded as a known quantity within the boundary layer. Here, the boundary layer is so thin that the pressure does not change across it. Furthermore, a crude estimate of τ_0, the wall shear stress,

can be made from the various scalings employed earlier: $\tau_0 \sim \mu U/\overline{\delta} \sim (\mu U/L)\text{Re}^{1/2}$. This implies a skin friction coefficient of

$$\frac{\tau_0}{\frac{1}{2}\rho U^2} \sim \frac{(\mu U/L)\sqrt{\text{Re}}}{\frac{1}{2}\rho U^2} = \frac{2}{\sqrt{\text{Re}}}.$$

This expression provides the correct order of magnitude and parametric dependence on Reynolds number. Only the numerical factor differs between different laminar boundary-layer flows.

9.2. BOUNDARY-LAYER THICKNESS DEFINITIONS

Since the fluid velocity in the boundary layer smoothly joins that of the outer flow, there is no obvious demarcation of the boundary layer's edge. Thus, a variety of thickness definitions are used to define a boundary layer's character. The three most common thickness definitions are described here.

The first, δ_{99}, is an overall boundary-layer thickness that specifies the distance from the wall where the stream-wise velocity in the boundary layer is $0.99U_e$, where U_e is the local free-stream speed. For a known boundary-layer stream-wise velocity profile, $u(x, y)$, at down-stream distance x, this thickness is defined by: $u(x, \delta_{99}) = 0.99U_e(x)$. This thickness primarily plays a conceptual role in boundary-layer research. In practice it is difficult to measure accurately, and its physical importance is subjective since the choice of 99% instead of 95%, 98%, 99.5%, or another percentage is arbitrary.

A second measure of the boundary-layer thickness, and one in which there is no arbitrariness, is the *displacement thickness*, which is commonly denoted δ^* or δ_1. It is defined as the thickness of a layer of zero-velocity fluid that has the same velocity deficit as the actual boundary layer. The velocity deficit in a boundary layer is $U_e - u$, so this definition implies

$$\int\limits_{y=0}^{h} (U_e - u)dy = \int\limits_{y=0}^{\delta^*} (U_e - 0)dy = U_e\delta^*, \text{ or } \delta^* = \int\limits_{y=0}^{\infty} \left(1 - \frac{u}{U_e}\right)dy, \qquad (9.16)$$

where h is a surface-normal distance that lies far outside the boundary layer (Figure 9.3). Here the extension $h \to \infty$ in the upper limit in the last integration is not problematic because $U_e - u \to 0$ exponentially fast as $y \to \infty$. Alternatively, the displacement thickness is the distance by which the wall would have to be displaced outward in a hypothetical frictionless flow to maintain the same mass flux as that in the actual flow. This means that the displacement thickness can be interpreted as the distance by which streamlines outside the boundary layer are displaced due to the presence of the boundary layer. Figure 9.4 shows the displacement of streamlines over a flat plate. Equating mass flux across two sections A and B, we obtain

$$U_e h = \int\limits_{y=0}^{h+\delta^*} u\,dy = \int\limits_{y=0}^{h} u\,dy + U_e\delta^*, \quad \text{or} \quad U_e\delta^* = \int\limits_{y=0}^{h} (U_e - u)dy,$$
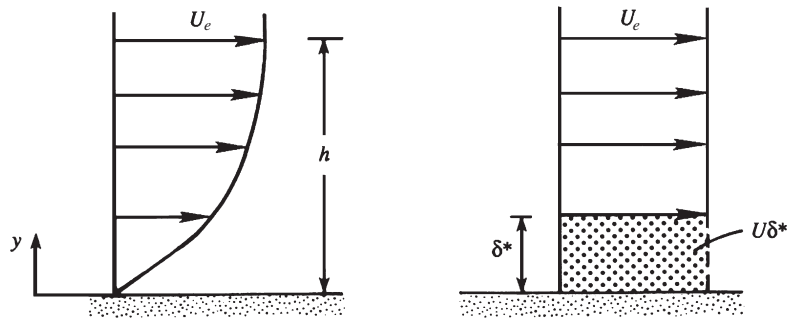
FIGURE 9.3   Schematic depiction of the displacement thickness. The panel on the left shows a typical laminar boundary-layer profile. The panel on the right shows an equivalent ideal-flow velocity profile with a zero-velocity layer having the same volume-flux deficit as the actual boundary layer. The thickness of this zero-velocity layer is the displacement thickness δ^*.

where h is the wall-normal distance defined above. Here again, it can be replaced by ∞ without changing the integral in the final equation, which then reduces to (9.16).

The displacement thickness is used in the design of airfoils, ducts, nozzles, intakes of air-breathing engines, wind tunnels, etc. by first assuming a frictionless flow and then revising the device's geometry to produce the desired flow condition with the boundary layer present. Here, the method for the geometric revisions involves using δ^* to correct the outer flow solution for the presence of the boundary layer. As mentioned in Section 9.1, the first approximation is to neglect the existence of the boundary layer, and calculate the ideal-flow dp/dx over the surface of interest. A solution of the boundary-layer equations gives $u(x,y)$, which can be integrated using (9.16) to find $\delta^*(x)$, the displacement thickness. The flow device's surface is then displaced outward by this amount and a next approximation of dp/dx is found from a solution for flow over the mildly revised geometry (see Exercise 9.22). Thus, $\delta^*(x)$ is
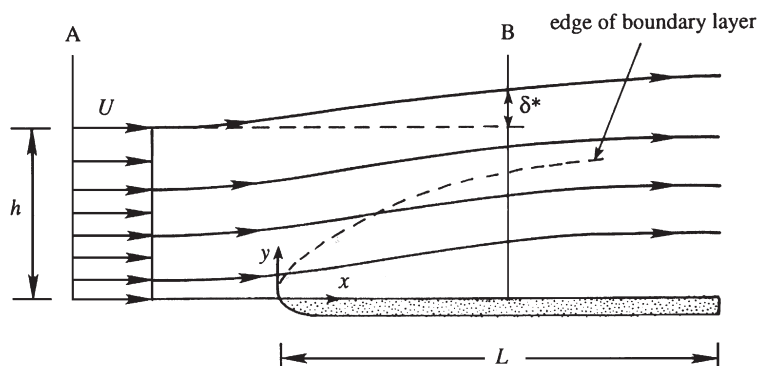

FIGURE 9.4   Displacement thickness and streamline displacement. Within the boundary layer, fluid motion in the downstream direction is retarded, that is, $\partial u/\partial x$ is negative. Thus, the continuity equation (6.2) requires $\partial v/\partial y$ to be positive, so the boundary layer produces a surface-normal velocity that deflects streamlines away from the surface. Above the boundary layer, the extent of this deflection is the displacement thickness δ^*.

a critical ingredient in such an iterative solution procedure that alternates between the outer- and inner-flow solutions.

A third measure of the boundary-layer thickness is the momentum thickness θ or δ_2. It is defined such that $\rho U^2 \theta$ is the momentum loss in the actual flow because of the presence of the boundary layer. A control volume calculation (see Exercise 9.6) leads to the following definition:

$$\theta = \int_{y=0}^{\infty} \frac{u}{U_e}\left(1 - \frac{u}{U_e}\right)dy. \tag{9.17}$$

The momentum thickness embodies the integrated signature of the wall shear stress from the beginning of the boundary layer to the stream-wise location of interest.

9.3. BOUNDARY LAYER ON A FLAT PLATE: BLASIUS SOLUTION

The simplest possible boundary layer forms on a semi-infinite flat plate with a constant free-stream flow speed, $U_e = U = \text{constant}$. In this case, the boundary-layer equations simplify to:

$$\frac{\partial u}{\partial x} + \frac{\partial v}{\partial y} = 0 \quad \text{and} \quad u\frac{\partial u}{\partial x} + v\frac{\partial u}{\partial y} = \nu\frac{\partial^2 u}{\partial y^2}, \tag{6.2, 9.18}$$

where (9.11) requires $dp/dx = 0$ because $dU_e/dx = 0$. Here, the independent variables are x and y, and the dependent field quantities are u and v. The flow is incompressible but rotational, so a guaranteed solution of (6.2) may be sought in terms of a stream function, ψ, with the two velocity components determined via derivatives of ψ (see (6.3)). Here, the flow is steady and there is no imposed length scale, so a similarity solution for ψ can be proposed based on (8.32) and (9.6):

$$\psi = U\delta(x)f(\eta) \quad \text{where } \eta = y/\delta(x), \tag{9.19}$$

where x is the time-like independent variable, f is an unknown dimensionless function, and $\delta(x)$ is a boundary-layer thickness that is to be determined as part of the solution (it is not a Dirac delta-function). Here the coefficient $U\delta$ in (9.19) has replaced $UA\xi^{-n}$ in (8.32) based on dimensional considerations; the stream function must have dimensions of length^2/ time. A more general form of (9.19) that uses UAx^{-n} as the coefficient of $f(\eta)$ produces the same results when combined with (9.18).

The solution to (6.2) and (9.18) should be valid for $x > 0$, so the boundary conditions are:

$$u = v = 0 \quad \text{on } y = 0, \tag{9.20}$$

$$u(x, y) \to U \quad \text{as } y/\delta \to \infty, \text{ and} \tag{9.21}$$

$$\delta \to 0 \quad \text{as } x \to 0. \tag{9.22}$$

Here we note that the boundary-layer approximation will not be valid near $x = 0$ (the leading edge of the plate) where the high Reynolds number approximation, $\text{Re}_x = Ux/\nu \gg 1$, used to reach (9.18) is not valid. Ideally, the exact equations of motion would be solved from $x = 0$ up some location, x_0, where $Ux_0/\nu \gg 1$. Then, the stream-wise velocity profile at this location

would be used in the inlet boundary condition (9.15), and (9.18) could be solved for $x > x_0$ to determine the boundary-layer flow. However, for this similarity solution, we are effectively assuming that the distance x_0 is small compared to x and can be ignored. Thus, the boundary condition (9.22), which replaces (9.15), is really an assumption that must be shown to produce self-consistent results when $\text{Re}_x \gg 1$.

The prior discussion touches on the question of a boundary layer's downstream dependence on, or memory of, its initial state. If the external stream $U_e(x)$ admits a similarity solution, is the initial condition forgotten? And, if so, how soon? Serrin (1967) and Peletier (1972) showed that for $U_e dU_e/dx > 0$ (*favorable* pressure gradients) and allowing similarity solutions, the initial condition is forgotten and the larger the free-stream acceleration the sooner similarity is achieved. However, a decelerating flow will accentuate details of the boundary layer's initial state and similarity will never be found even if it is mathematically possible. This is consistent with the experimental findings of Gallo et al. (1970). Interestingly, a flat plate for which $U_e(x) = U = \text{const.}$ is the borderline case; similarity is eventually achieved. Thus, a solution in the form (9.19) is pursued here.

The first solution's steps involve performing derivatives of ψ to find u and v:

$$u = \frac{\partial \psi}{\partial y} = U\delta \frac{df}{d\eta}\frac{1}{\delta} = Uf',$$

$$v = -\frac{\partial \psi}{\partial x} = -U\left(\frac{d\delta}{dx}f + \delta\frac{df}{d\eta}\left(-\frac{y}{\delta^2}\right)\frac{d\delta}{dx}\right) = U\delta'(-f + \eta f'),$$

(9.23, 9.24)

where a prime denotes differentiation of a function with respect to its argument. When substituted into (9.18), these produce:

$$Uf'Uf''\left(-\frac{y}{\delta^2}\right)\delta' + U\delta'(-f + \eta f')\frac{U}{\delta}f'' = v\frac{U}{\delta^2}f''', \text{ or}$$

$$\left[-\frac{U^2}{\delta}\delta'\right]\eta f'f'' - \left[\frac{U^2}{\delta}\delta'\right]ff'' + \left[\frac{U^2}{\delta}\delta'\right]\eta f'f'' = \left[v\frac{U}{\delta^2}\right]f'''.$$

The first and third terms on the left are equal and opposite, so (9.18) finally reduces to:

$$-\left[\frac{U^2}{\delta}\delta'\right]ff'' = \left[v\frac{U}{\delta^2}\right]f'''.$$

(9.25)

For a similarity solution, the coefficients in [,]-braces must be proportional:

$$C\frac{U^2}{\delta}\delta' = v\frac{U}{\delta^2} \rightarrow C\delta\frac{d\delta}{dx} = \frac{v}{U} \rightarrow C\frac{\delta^2}{2} = \frac{vx}{U} + D,$$

where C and D are constants. Here (9.22) requires $D = 0$, and C can be chosen equal to 2 to simplify the resulting expression for δ:

$$\delta(x) = [vx/U]^{1/2}.$$

(9.26)

As described above, this result will be imperfect as $x \to 0$ since it is based on equations that are only valid when $\text{Re}_x \gg 1$. However, it is self-consistent since it produces a boundary

FIGURE 9.5   The Blasius similarity solution of velocity distribution in a laminar boundary layer on a flat plate with zero-pressure gradient, $U_e = U = $ constant.   The finite slope at $\eta = 0$ implies a nonzero wall shear stress τ_0. The boundary layer's velocity profile smoothly asymptotes to U as $\eta \to \infty$. The momentum θ and displacement δ^* thicknesses are indicated by arrows on the horizontal axis.
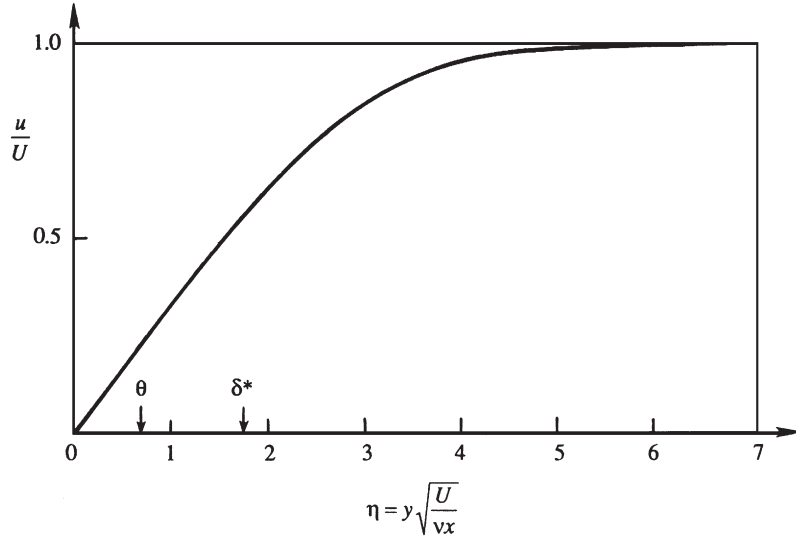
layer that thins with decreasing distance so that $u \to U$ as $x \to 0$. When (9.26) is substituted into (9.25), the final equation for f is found:

$$\frac{d^3f}{d\eta^3} + \frac{1}{2}f\frac{d^2f}{d\eta^2} = 0, \quad \text{or} \quad f''' + \frac{1}{2}ff'' = 0. \tag{9.27}$$

The boundary conditions for (9.27) are:

$$df/d\eta = 0 \quad \text{and} \quad f = 0 \quad \text{at } \eta = 0, \text{ and} \tag{9.28}$$
$$df/d\eta \to 1 \quad \text{as } \eta \to \infty, \tag{9.29}$$

which replace (9.20) and (9.21), respectively.

A series solution of (9.27), subject to (9.28) and (9.29), was given by Blasius; today it is much easier to numerically determine $f(\eta)$. The resulting profile of $u/U = f'(\eta)$ is shown in Figure 9.5. The solution makes the profiles at various downstream distances collapse into a single curve of u/U vs. $y[U/\nu x]^{1/2}$, and is in excellent agreement with experimental data for laminar flow at high Reynolds numbers. The profile has a point of inflection (i.e., zero curvature) at the wall, where $\partial^2 u/\partial y^2 = 0$. This is a result of the absence of a pressure gradient in the flow (see Section 9.7).

The Blasius boundary-layer profile has a variety of noteworthy properties. First of all, an asymptotic analysis of the solution to (9.27) shows that $(df/d\eta - 1) \sim (1/\eta)\exp(-\eta^2/4)$ as $\eta \to \infty$ so u approaches U very smoothly with increasing wall-normal distance. Second, the wall-normal velocity is:

$$v = -\frac{\partial \psi}{\partial x} = \frac{1}{2}\sqrt{\frac{\nu U}{x}}\left(-f + \eta\frac{df}{d\eta}\right), \quad \text{or} \quad \frac{v}{U} = \frac{1}{2\text{Re}_x^{1/2}}\left(-f + \eta\frac{df}{d\eta}\right) \sim \frac{0.86}{\text{Re}_x^{1/2}} \quad \text{as } \eta \to \infty,$$
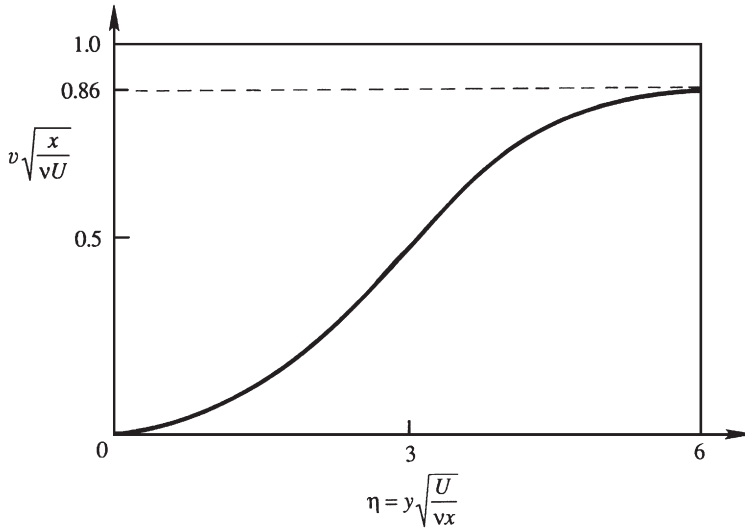
FIGURE 9.6 Surface-normal velocity component, v, in a laminar boundary layer on a flat plate with constant free-stream speed U. Here the scaling on the vertical axis, $(v/U)\sqrt{\mathrm{Re}_x}$, causes it to be expanded compared to that in Figure 9.5.

a plot of which is shown in Figure 9.6. The wall-normal velocity increases from zero at the wall to a maximum value at the edge of the boundary layer, a pattern that is in agreement with the streamline shapes sketched in Figure 9.4.

The various thicknesses for the Blasius boundary layer are as follows. From Figure 9.5, the distance where $u = 0.99U$ is $\eta = 4.93$, so

$$\delta_{99} = 4.93\sqrt{\nu x/U} \quad \text{or} \quad \delta_{99}/x = 4.93/\mathrm{Re}_x^{1/2}. \tag{9.30}$$

The half-power boundary-layer thickness dependence, $\delta \sim x^{1/2}$, is in good agreement with experiments. For air at ordinary temperatures flowing at $U = 1$ m/s, the Reynolds number at a distance of 1 m from leading edge of a flat plate is $\mathrm{Re}_x = 6 \times 10^4$, and (9.30) gives $\delta_{99} = 2$ cm, showing that the boundary layer is indeed thin. The displacement and momentum thicknesses, (9.16) and (9.17), of the Blasius boundary layer are

$$\delta^* = 1.72\sqrt{\nu x/U}, \quad \text{and} \quad \theta = 0.664\sqrt{\nu x/U}.$$

These thicknesses are indicated along the abscissa of Figure 9.5.

The local wall shear stress is $\tau_0 = \mu(du/dy)_{y=0} = (\mu U/\delta)(d^2f/d\eta^2)_{\eta=0}$, or

$$\tau_0 = 0.332\rho U^2/\sqrt{\mathrm{Re}_x}. \tag{9.31}$$

The wall shear stress therefore decreases as $x^{-1/2}$, a result of the thickening of the boundary layer and the associated decrease of the velocity gradient at the surface. Note that the wall shear stress at the plate's leading edge has an integrable singularity. This is a manifestation of the fact that boundary-layer theory breaks down near the leading edge where the assumptions $\mathrm{Re}_x \gg 1$ and $\partial/\partial x \ll \partial/\partial y$ are invalid. The wall shear stress is commonly expressed in terms of the dimensionless *skin friction coefficient*:

$$C_f \equiv \frac{\tau_0}{\frac{1}{2}\rho U^2} = \frac{0.664}{\sqrt{\text{Re}_x}}. \tag{9.32}$$

The drag force per unit width on one side of a plate of length L is

$$F_D = \int_0^L \tau_0 dx = \frac{0.664\rho U^2 L}{\sqrt{\text{Re}_L}},$$

where $\text{Re}_L \equiv UL/\nu$ is the Reynolds number based on the plate length. This equation shows that the drag force is proportional to the 3/2 power of velocity. This should be compared with small Reynolds number flows, where the drag is proportional to the first power of velocity. We shall see later in this chapter that the drag on a *blunt* body in a high Reynolds number flow is proportional to the *square* of velocity.

The overall *drag coefficient* for one side of the plate, defined in the usual manner, is

$$C_D = \frac{F_D}{\frac{1}{2}\rho U^2 L} = \frac{1.33}{\sqrt{\text{Re}_L}}. \tag{9.33}$$

It is clear from (9.32) and (9.33) that

$$C_D = \frac{1}{L}\int_0^L C_f dx,$$

which says that the overall drag coefficient is the spatial average of the local skin friction coefficient. However, carrying out an integration from $x = 0$ may be of questionable validity because the equations and solutions are valid only for $\text{Re}_x \gg 1$. Nevertheless, (9.33) is found to be in good agreement with laminar flow experiments for $\text{Re}_L > 10^3$.

9.4. FALKNER-SKAN SIMILARITY SOLUTIONS OF THE LAMINAR BOUNDARY-LAYER EQUATIONS

The Blasius boundary-layer solution is one of a whole class of similarity solutions to the boundary-layer equations that were investigated by Falkner and Skan (1931). In particular, similarity solutions of (6.2), (9.9), and (9.10) are possible when $U_e(x) = ax^n$, and $\text{Re}_x = ax^{(n+1)}/\nu$ is sufficiently large so that the boundary-layer approximation is valid and any dependence on an initial velocity profile has been forgotten. In this case, the initial location x_0 again disappears from the problem and a similarity solution may be sought in the form:

$$\psi(x, y) = \sqrt{\nu x U_e(x)} f(\eta), \quad \text{where } \eta = \frac{y}{\delta(x)} = \frac{y}{x}\sqrt{\text{Re}_x} = y\sqrt{\frac{a}{\nu}} x^{(n-1)/2}. \tag{9.34}$$

This is a direct extension of (9.19) to boundary-layer flow with a spatially varying free-stream speed $U_e(x)$. Here, $u/U_e = f'(\eta)$ as in the Blasius solution, but now the pressure gradient is nontrivial:

$$-dp/dx = U_e(dU_e/dx) = na^2 x^{2n-1}, \tag{9.35}$$

and the generic boundary-layer thickness is

$$\delta(x) = \sqrt{vx/U_e(x)} = \sqrt{vx^{1-n}/a},$$

which increases in size when $n < 1$ and decreases in size when $n > 1$ as x increases. When $n = 1$, then $\delta(x)$ is constant. Substituting (9.34) and (9.35) into (9.9) allows it to be reduced to the similarity form:

$$\frac{d^3f}{d\eta^3} + \frac{n+1}{2} f \frac{d^2f}{d\eta^2} - n\left(\frac{df}{d\eta}\right)^2 + n = 0, \quad \text{or} \quad f''' + \frac{n+1}{2} ff'' - nf'^2 + n = 0, \tag{9.36}$$

where f is subject to the boundary conditions (9.28) and (9.29). The Blasius equation (9.27) is a special case of (9.36) for $n = 0$, that is, $U_e(x) = U = $ constant.

Solutions to (9.36) are displayed in Figure 5.9.1 of Batchelor (1967) and are reproduced here in Figure 9.7. They are parameterized by the power law exponent, n, which also sets the pressure gradient. The shapes of the various profiles can be understood by comparing them to the stream-wise velocity profiles obtained for flow between parallel plates when the upper plate moves with a positive horizontal velocity. They show a monotonically increasing shear stress [$f''(0)$] as n increases. When n is positive, the flow accelerates as it moves to higher x, the pressure gradient is *favorable* ($dp/dx < 0$), the wall shear stress is nonzero and positive, and $(\partial^2 u/\partial y^2)_{y\,=\,0} < 0$. Thus, the profiles for $n > 0$ in Figure 9.7 are similar to the lower half of the profiles shown in Figures 8.4a and 8.4d. When $n = 0$, there is no flow acceleration or pressure gradient and $(\partial^2 u/\partial y^2)_{y\,=\,0} = 0$. This case corresponds
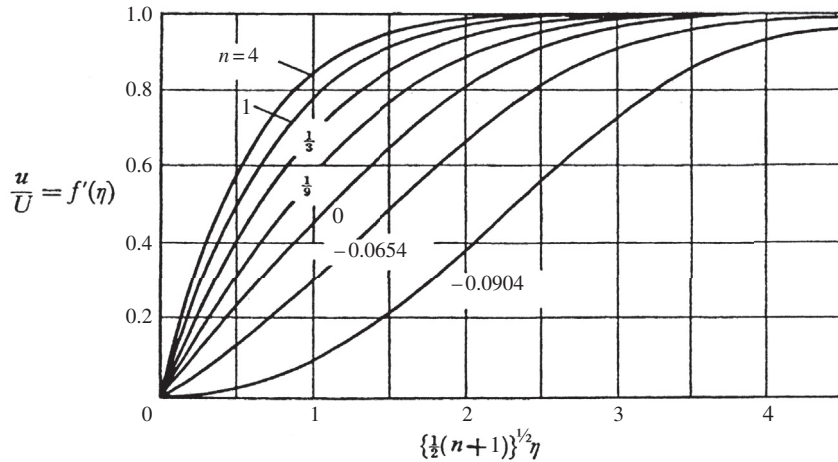

FIGURE 9.7 Falkner-Skan profiles of stream-wise velocity in a laminar boundary layer when the external stream is $U_e = ax^n$. The horizontal axis is the scaled surface-normal coordinate. The various curves are labeled by their associated value of n. When $n > 0$, the free-stream speed increases with increasing x, and $\partial^2 u/\partial y^2$ is negative throughout the boundary layer. When $n = 0$ (the Blasius boundary layer), the free-stream speed is constant, and $\partial^2 u/\partial y^2 = 0$ at the wall and is negative throughout the boundary layer. When $n < 0$, the free-stream speed decreases with increasing x, and $\partial^2 u/\partial y^2$ is positive near the wall but negative higher up in the boundary layer so there is an inflection point in the stream-wise velocity profile at a finite distance from the surface. *Reprinted with the permission of Cambridge University Press, from: G. K. Batchelor,* An Introduction to Fluid Dynamics, *1st ed. (1967).*

to Figure 8.4c. When n is negative, the flow decelerates as it moves downstream, the pressure gradient is *adverse* ($dp/dx > 0$), the wall shear stress may approach zero, and $(\partial^2 u/\partial y^2)_{y\,=\,0} < 0$. Thus, the profiles for $n < 0$ in Figure 9.7 approach that shown in Figure 8.4b. For $n = -0.0904$, $f''(0) = 0$, so $\tau_0 = 0$, and boundary-layer separation is imminent all along the surface. Solutions of (9.36) exist for $n < -0.0904$ but these solutions involve reverse flow, like that shown in Figure 8.4b, and do not necessarily represent boundary layers because the stream-wise velocity scaling in (9.6) used to reach (9.9), $u \sim U$, is invalid when $u = 0$ away from the wall.

In many real flows, boundary or initial conditions prevent similarity solutions from being directly applicable. However, after a variety of empirical and analytical advances made in the middle of the twentieth century, useful approximate methods were found to predict the properties of laminar boundary layers. These approximate techniques are based on the von Karman boundary-layer integral equation, which is derived in the next section. Then, in Section 9.6, the Thwaites method for estimating the surface shear stress, the displacement thickness, and the momentum thickness for attached laminar boundary layers is presented. In the most general cases or when greater accuracy is required, the boundary-layer equations with boundary and initial conditions as written in (6.2) and (9.9) through (9.15) must be solved by procedures that are discussed in more detail in the next chapter.

9.5. VON KARMAN MOMENTUM INTEGRAL EQUATION

Exact solutions of the boundary-layer equations are possible only in simple cases. In more complicated problems, approximate methods satisfy only an *integral* of the boundary-layer equations across the layer thickness. When this integration is performed, the resulting ordinary differential equation involves the boundary layer's displacement and momentum thicknesses, and its wall shear stress. This simple differential equation was derived by von Karman in 1921 and applied to several situations by Pohlhausen (1921).

The common emphasis of an integral formulation is to obtain critical information with minimum effort. The important results of boundary-layer calculations are the wall shear stress, displacement thickness, momentum thickness, and separation point (when one exists). The von Karman boundary-layer momentum integral equation explicitly links the first three of these, and can be used to estimate, or at least determine the existence of, the fourth. The starting points are (6.2) and (9.9), with the pressure gradient specified in terms of $U_e(x)$ from (9.11) and the shear stress $\tau = \mu(\partial u/\partial y)$:

$$u\frac{\partial u}{\partial x} + v\frac{\partial u}{\partial y} = U_e\frac{dU_e}{dx} + \frac{1}{\rho}\frac{\partial \tau}{\partial y}. \tag{9.37}$$

Multiply (6.2) by u and add it to the left side of this equation:

$$u\left(\frac{\partial u}{\partial x} + \frac{\partial v}{\partial y}\right) + u\frac{\partial u}{\partial x} + v\frac{\partial u}{\partial y} = \frac{\partial(u^2)}{\partial x} + \frac{\partial(vu)}{\partial y} = U_e\frac{dU_e}{dx} + \frac{1}{\rho}\frac{\partial \tau}{\partial y}. \tag{9.38}$$

Move the term involving U_e to the other side of the last equality, and integrate (6.2) and (9.38) from $y = 0$ where $u = v = 0$ to $y = \infty$ where $u = U_e$ and $v = v_\infty$:

$$\int\limits_0^\infty \left(\frac{\partial u}{\partial x} + \frac{\partial v}{\partial y} \right) dy = 0 \rightarrow \int\limits_0^\infty \frac{\partial u}{\partial x} dy = - \int\limits_0^\infty \frac{\partial v}{\partial y} dy = -[v]_0^\infty = -v_\infty, \tag{9.39}$$

$$\int\limits_0^\infty \left(\frac{\partial (u^2)}{\partial x} + \frac{\partial (vu)}{\partial y} - U_e \frac{dU_e}{dx} \right) dy$$

$$= +\frac{1}{\rho} \int\limits_0^\infty \frac{\partial \tau}{\partial y} dy \rightarrow \int\limits_0^\infty \left(\frac{\partial (u^2)}{\partial x} - U_e \frac{dU_e}{dx} \right) dy + U_e v_\infty = -\frac{1}{\rho} \tau_0, \tag{9.40}$$

where τ_0 is the shear stress at $y = 0$ and $\tau = 0$ at $y = \infty$. Use the final form of (9.39) to eliminate v_∞ from (9.40), and exchange the order of integration and differentiation in the first term of (9.40):

$$\frac{d}{dx} \int\limits_0^\infty u^2 dy - \int\limits_0^\infty U_e \frac{dU_e}{dx} dy - U_e \int\limits_0^\infty \frac{\partial u}{\partial x} dy = -\frac{1}{\rho} \tau_0. \tag{9.41}$$

Now, note that

$$U_e \int\limits_0^\infty \frac{\partial u}{\partial x} dy = U_e \frac{d}{dx} \int\limits_0^\infty u dy = \frac{d}{dx} \left(U_e \int\limits_0^\infty u dy \right) - \frac{dU_e}{dx} \int\limits_0^\infty u dy,$$

and use this to rewrite the third term on the left side of (9.41) to find:

$$\frac{d}{dx} \int\limits_0^\infty \left(u^2 - U_e u \right) dy + \frac{dU_e}{dx} \int\limits_0^\infty (u - U_e) dy = -\frac{1}{\rho} \tau_0. \tag{9.42}$$

A few final algebraic rearrangements produce:

$$\frac{1}{\rho} \tau_0 = \frac{d}{dx} \left[U_e^2 \int\limits_0^\infty \frac{u}{U_e} \left(1 - \frac{u}{U_e} \right) dy \right] + \frac{dU_e}{dx} U_e \int\limits_0^\infty \left(1 - \frac{u}{U_e} \right) dy, \text{ or}$$

$$\frac{1}{\rho} \tau_0 = \frac{d}{dx} [U_e^2 \theta] + U_e \delta^* \frac{dU_e}{dx}. \tag{9.43}$$

Throughout these manipulations, U_e and dU_e/dx may be moved inside or taken outside the vertical-direction integrations because they only depend on x.

Equation (9.43) is known as the *von Karman boundary-layer momentum integral equation*, and it is valid for steady laminar boundary layers and for time-averaged flow in turbulent boundary layers. It is a single ordinary differential equation that relates three unknowns θ, δ^*, and τ_0, so additional assumptions must be made or correlations provided to obtain solutions for these parameters. The search for appropriate assumptions and empirical correlations was

actively pursued by many researchers in the middle of the twentieth century starting with Pohlhausen (1921) and ending with Thwaites (1949) who combined analysis and inspired guesswork with the laminar boundary-layer measurements and equation solutions known at that time to develop the approximate empirical laminar-boundary-layer solution procedure for (9.43) described in the next section.

9.6. THWAITES' METHOD

To solve (9.43) at least two additional equations are needed. Using the correlation parameter,

$$\lambda \equiv \frac{\theta^2}{\nu}\frac{dU_e}{dx}, \tag{9.44}$$

introduced by Holstein and Bohlen (1940), Thwaites (1949) developed an approximate solution to (9.43) that involves two empirical dimensionless functions $l(\lambda)$ and $H(\lambda)$,

$$\tau_0 \equiv \mu\frac{U_e}{\theta}l(\lambda) \quad \text{and} \quad \frac{\delta^*}{\theta} \equiv H(\lambda), \tag{9.45, 9.46}$$

that are listed in Table 9.1. This tabulation is identical to Thwaites' original for $\lambda \geq -0.060$ but includes the improvements recommended by Curle and Skan a few years later (see Curle, 1962) for $\lambda < -0.060$. The function $l(\lambda)$ is sometimes known as the shear correlation while $H(\lambda)$ is commonly called the shape factor.

Thwaites' method is developed from (9.43) by multiplying it with $\rho\theta/\mu U_e$:

$$\frac{\theta\tau_0}{\mu U_e} = \frac{\rho\theta}{\mu U_e}\frac{d}{dx}(U_e^2\theta) + \frac{\rho\theta}{\mu U_e}U_e\delta^*\frac{dU_e}{dx}, \quad \text{or} \quad \frac{\theta\tau_0}{\mu U_e} = 2\frac{\theta^2}{\nu}\frac{dU_e}{dx} + \frac{U_e\theta}{\nu}\frac{d\theta}{dx} + \frac{\theta^2}{\nu}\frac{\delta^*}{\theta}\frac{dU_e}{dx}. \tag{9.47}$$

The definitions of l and H allow the second equation of (9.47) to be simplified:

$$l(\lambda) = (2 + H(\lambda))\frac{\theta^2}{\nu}\frac{dU_e}{dx} + \frac{U_e}{2}\frac{d}{dx}\left(\frac{\theta^2}{\nu}\right).$$

The momentum thickness θ can be eliminated from this equation using (9.44), to find:

$$U_e\frac{d}{dx}\left(\frac{\lambda}{dU_e/dx}\right) = 2l(\lambda) - 2(2 + H(\lambda))\lambda \equiv L(\lambda). \tag{9.48}$$

Fortunately, $L(\lambda) \approx 0.45 - 6.0\lambda = 0.45 + 6.0m$ is approximately linear as shown in Figure 9.8 which is taken from Thwaites' (1949) original paper where $m = -\lambda$. With this linear fit, (9.48) can be integrated:

$$U_e\frac{d}{dx}\left(\frac{\lambda}{dU_e/dx}\right) = 0.45 - 6.0\lambda \rightarrow \frac{d}{dx}\left(\frac{\theta^2}{\nu}\right) + \frac{6.0}{U_e}\frac{dU_e}{dx}\frac{\theta^2}{\nu} = \frac{0.45}{U_e}. \tag{9.49}$$

The second version of (9.49) is a first-order linear inhomogeneous differential equation for θ^2/ν; its integrating factor is U_e^6. The resulting solution for θ^2 involves a simple

TABLE 9.1 Universal Functions for Thwaites' Method

| λ	$l(\lambda)$	$H(\lambda)$
0.25	0.500	2.00
0.20	0.463	2.07
0.14	0.404	2.18
0.12	0.382	2.23
0.10	0.359	2.28
0.08	0.333	2.34
0.064	0.313	2.39
0.048	0.291	2.44
0.032	0.268	2.49
0.016	0.244	2.55
0	0.220	2.61
−0.008	0.208	2.64
−0.016	0.195	2.67
−0.024	0.182	2.71
−0.032	0.168	2.75
−0.040	0.153	2.81
−0.048	0.138	2.87
−0.052	0.130	2.90
−0.056	0.122	2.94
−0.060	0.113	2.99
−0.064	0.104	3.04
−0.068	0.095	3.09
−0.072	0.085	3.15
−0.076	0.072	3.22
−0.080	0.056	3.30
−0.084	0.038	3.39
−0.086	0.027	3.44
−0.088	0.015	3.49
−0.090	0	3.55
	(Separation)	
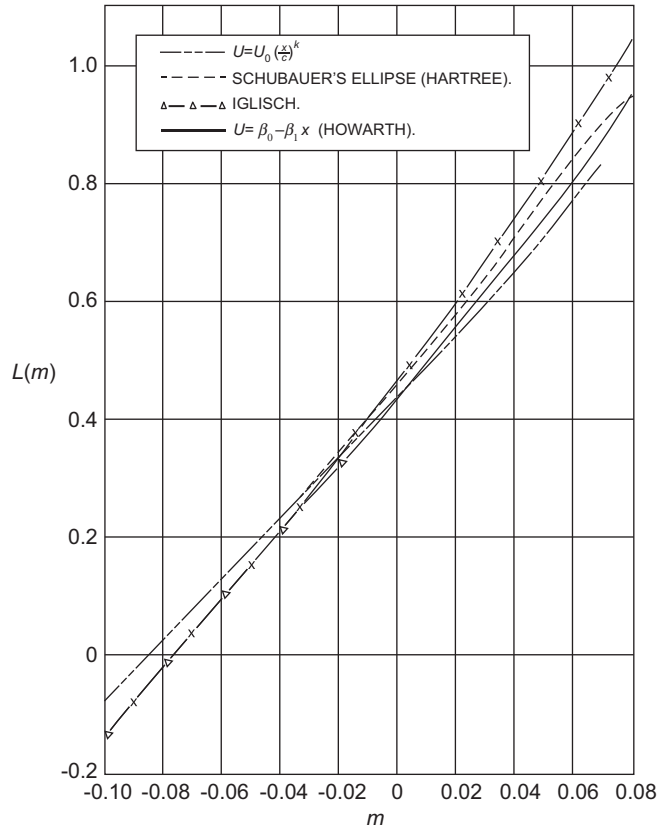
FIGURE 9.8   Plot of $L(m)$ from (9.48) vs. $m = -\lambda$ from Thwaites' 1949 paper. Here a suitable empirical fit to the four sources of laminar boundary-layer data is provided by $L(m) = 0.45 + 6.0m = 0.45 - 6.0\lambda$. *Reprinted with the permission of The Royal Aeronautical Society.*

integral of the fifth power of the free-stream velocity at the edge of the boundary layer:

$$\frac{\theta^2 U_e^6(x)}{\nu} = 0.45 \int_0^x U_e^5(x')\, dx' + \frac{\theta_0^2 U_0^6}{\nu} \quad \text{or} \quad \theta^2 = \frac{0.45\nu}{U_e^6(x)} \int_0^x U_e^5(x')\ dx' + \frac{\theta_0^2 U_0^6}{U_e^6(x)}, \tag{9.50}$$

where x' is an integration variable, $\theta = \theta_0$, and $U_e = U_0$ at $x = 0$. If $x = 0$ is a stagnation point ($U_e = 0$), then $\theta_0 = 0$. Once the integration specified by (9.50) is complete, the surface shear stress and displacement thickness can be recovered by computing λ and then using (9.45), (9.46), and Table 9.1. Overall, the accuracy of Thwaites' method is $\pm 3\%$ or so for favorable pressure gradients, and $\pm 10\%$ for adverse pressure gradients but perhaps slightly worse near boundary-layer separation. The great strength of Thwaites' method is that it involves only one parameter (λ) and requires only a single integration. This simplicity makes it ideal

for preliminary engineering calculations that are likely to be followed by more formal computations or experiments.

Before proceeding to example calculations, an important limitation of boundary-layer calculations that start from a steady presumed surface pressure distribution (such as Thwaites' method) must be stated. Such techniques can only predict the existence of boundary-layer separation; they do not reliably predict the location of boundary-layer separation. As will be further discussed in the next section, once a boundary layer separates from the surface on which it has formed, the fluid mechanics of the situation are entirely changed. First of all, the boundary-layer approximation is invalid downstream of the separation point because the layer is no longer thin and contiguous to the surface; thus, the scaling (9.6) is no longer valid. Second, separation commonly leads to unsteadiness because separated boundary layers are unstable and may produce fluctuations even if all boundary conditions are steady. And third, a separated boundary layer commonly has an enormous flow-displacement effect that drastically changes the outer flow so that it no longer imposes the presumed attached boundary-layer surface pressure distribution. Thus, any boundary-layer calculation that starts from a presumed surface pressure distribution should be abandoned once that calculation predicts the occurrence of boundary-layer separation.

The following two examples illustrate the use of Thwaites' method with and without a prediction of boundary-layer separation.

EXAMPLE 9.1

Use Thwaites' method to estimate the momentum thickness, displacement thickness, and wall shear stress of the Blasius boundary layer with $\theta_0 = 0$ at $x = 0$.

Solution

The solution plan is to use (9.50) to obtain θ. Then, because $dU_e/dx = 0$ for the Blasius boundary layer, $\lambda = 0$ at all downstream locations and the remaining boundary-layer parameters can be determined from the θ results, (9.45), (9.46), and Table 9.1. The first step is setting $U_e = U = $ constant in (9.50) with $\theta_0 = 0$:

$$\theta^2 = \frac{0.45\nu}{U^6} \int_0^x U^5 dx = \frac{0.45\nu}{U}x, \quad \text{or} \quad \theta = 0.671\sqrt{\frac{\nu x}{U}}.$$

This approximate answer is only 1% higher than the Blasius-solution value. For $\lambda = 0$, the tabulated shape factor is $H(0) = 2.61$, so

$$\delta^* = \theta\left(\frac{\delta^*}{\theta}\right) = \theta H(0) = 0.671\sqrt{\frac{\nu x}{U}}(2.61) = 1.75\sqrt{\frac{\nu x}{U}}.$$

This approximate answer is less than 2% higher than the Blasius-solution value. For $\lambda = 0$, the shear correlation value is $l(0) = 0.220$, so

$$\tau_0 = \mu\frac{U}{\theta}l(0) = \frac{\mu U}{0.671\sqrt{\nu x/U}}(0.220) = \frac{1}{2}\rho U^2(0.656)\sqrt{\frac{\nu}{Ux}},$$

which implies a skin friction coefficient of

$$C_f = \frac{\tau_0}{\frac{1}{2}\rho U^2} = \frac{0.656}{\sqrt{Re_x}},$$

which is only 1.2% below the Blasius-solution value.

EXAMPLE 9.2

A shallow-angle, two-dimensional diffuser of length L is designed for installation downstream of a blower in a ventilation system to slow the blower-outlet airflow via an increase in duct cross-sectional area (see Figure 9.9). If the diffuser should reduce the flow speed by half by doubling the flow area and the boundary layer is laminar, is boundary-layer separation likely to occur in this diffuser?

Solution

The first step is to determine the outer flow $U_e(x)$ by assuming uniform (ideal) flow within the diffuser. Then, (9.49) can be used to estimate $\theta^2(x)$ and $\lambda(x)$. Boundary-layer separation will occur if λ falls below -0.090.

For uniform incompressible flow within the diffuser: $U_1A_1 = U_e(x)A(x)$, where (1) denotes the diffuser inlet, $U_e(x)$ is the flow speed, and $A(x)$ is the cross-sectional area. For flat diffuser sides, a doubling of the flow area in a distance L requires $A(x) = A_1(1 + x/L)$, so the ideal outer flow velocity is $U_e(x) = U_1(1 + x/L)^{-1}$. With this exterior velocity the Thwaites' integral becomes:

$$\theta^2 = \frac{0.45\nu}{U_e^6(x)} \int_0^x U_e^5(x')\, dx' + \frac{\theta_0^2 U_0^6}{U_e^6(x)} = \frac{0.45\nu}{U_1}\left(1 + \frac{x}{L}\right)^6 \int_0^x \left(1 + \frac{x}{L}\right)^{-5} dx + \theta_0^2\left(1 + \frac{x}{L}\right)^6,$$

where $U_0 = U_1$ in this case. The 0-to-x integration is readily completed and this produces:

$$\theta^2 = \frac{0.45\nu}{U_1}\left(1 + \frac{x}{L}\right)^6 \frac{L}{4}\left[1 - \left(1 + \frac{x}{L}\right)^{-4}\right] + \theta_0^2\left(1 + \frac{x}{L}\right)^6.$$

From this equation it is clear that θ grows with increasing x. This relationship can be converted to λ by multiplying it with $(1/\nu)dU_e/dx = -(U_1/\nu L)(1 + x/L)^{-2}$:
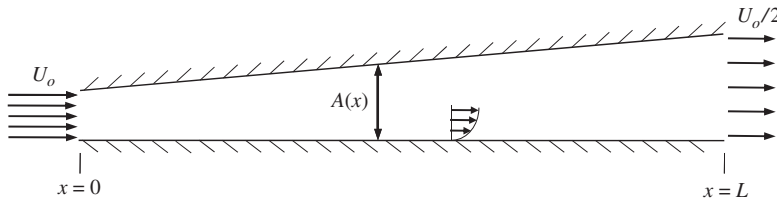

FIGURE 9.9 A simple two-dimensional diffuser of length L intended to slow the incoming flow to half its speed by doubling the flow area. The resulting adverse pressure gradient in the diffuser influences the character of the boundary layers that develop on the diffuser's inner surfaces, especially when these boundary layers are laminar.

$$\lambda = \frac{\theta^2}{\nu}\frac{dU_e}{dx} = -\frac{0.45}{4}\left[\left(1+\frac{x}{L}\right)^4 - 1\right] - \frac{\theta_0^2 U_1}{\nu L}\left(1+\frac{x}{L}\right)^4.$$

Here, we can see that even when $\theta_0 = 0$, λ will (at best) start at zero and become increasingly negative with increasing x. At this point, a determination of whether or not boundary-layer separation will occur involves calculating λ as a function of x/L. The following table comes from evaluating the last equation with $\theta_0 = 0$.

x/L	λ
0	0
0.05	−0.02424
0.1	−0.05221
0.15	−0.08426
0.2	−0.12078

Here, Thwaites' method predicts that boundary-layer separation will occur, since λ will fall below −0.090 at $x/L \approx 0.16$, a location that is far short of the end of the diffuser at $x = L$. While it is tempting to consider this a prediction of the location of boundary-layer separation, such a temptation should be avoided. In addition, if θ_0 was nonzero, then λ would decrease even more quickly than shown in the table, making the positive prediction of boundary-layer separation even more firm. (In reality, diffusers in duct work and flow systems are common but they typically operate with turbulent boundary layers that more effectively resist separation.)

9.7. TRANSITION, PRESSURE GRADIENTS, AND BOUNDARY-LAYER SEPARATION

The analytical and empirical results provided in the prior sections are altered when a boundary layer transitions from laminar to turbulent flow, and when a boundary layer separates from the surface on which it has developed. Both of these phenomena, especially the second, are influenced by the pressure gradient felt by the boundary layer.

The process of changing from laminar to turbulent flow is called *transition*, and it occurs in a wide variety of flows as the Reynolds number increases. For the present purposes, the complicated phenomenon known as *boundary-layer transition* is described in general terms. Interestingly for a high Reynolds number theory, the agreement of solutions to the laminar boundary equations with experimental data breaks down when the downstream-distance-based Reynolds number Re_x is larger than some critical value, say Re_{cr}, that depends on fluctuations in the free stream above the boundary layer and on the surface shape, curvature, roughness, vibrations, and pressure gradient. Above Re_{cr}, a laminar boundary-layer flow becomes unstable and transitions to turbulence. Typically, the critical Reynolds number decreases when the surface roughness or free-stream fluctuation levels increase. In general, Re_{cr} varies greatly and detailed predictions of transition are often a difficult task or research

endeavor. Within a factor of five or so, the transition Reynolds number for a smooth, flat-plate boundary layer is found to be

$$\mathrm{Re}_{cr} \sim 10^6 \ (\text{flat plate}).$$

Figure 9.10 schematically depicts the flow regimes on a semi-infinite flat plate (with the vertical direction greatly exaggerated). In the leading-edge region, $\mathrm{Re}_x = Ux/\nu \sim 1$, the full Navier-Stokes equations are required to properly describe the flow. As Re_x increases toward the downstream limit of the leading-edge region, we can locate x_0 as the maximal upstream location where the laminar boundary-layer equations are valid. For some distance $x > x_0$, the boundary layer's condition at $x = x_0$ is remembered. Eventually, the influence of the initial condition may be neglected and the solution becomes of similarity form. For somewhat larger Re_x, a bit farther downstream, an initial instability appears and fluctuations of a specific wavelength or frequency may be amplified. With increasing downstream distance, a wider spatial or temporal frequency range of fluctuations may be amplified and these fluctuations interact with each other nonlinearly through the advective acceleration terms in the momentum equation. As Re_x increases further, the fluctuations may increase in strength and the flow becomes increasingly chaotic and irregular with increasing downstream distance. When the fluctuations cease their rapid growth, the flow is said to be fully turbulent and transition is complete.

Laminar and turbulent boundary layers differ in many important ways. A fully turbulent boundary layer produces significantly more average surface shear stress τ_0 than an
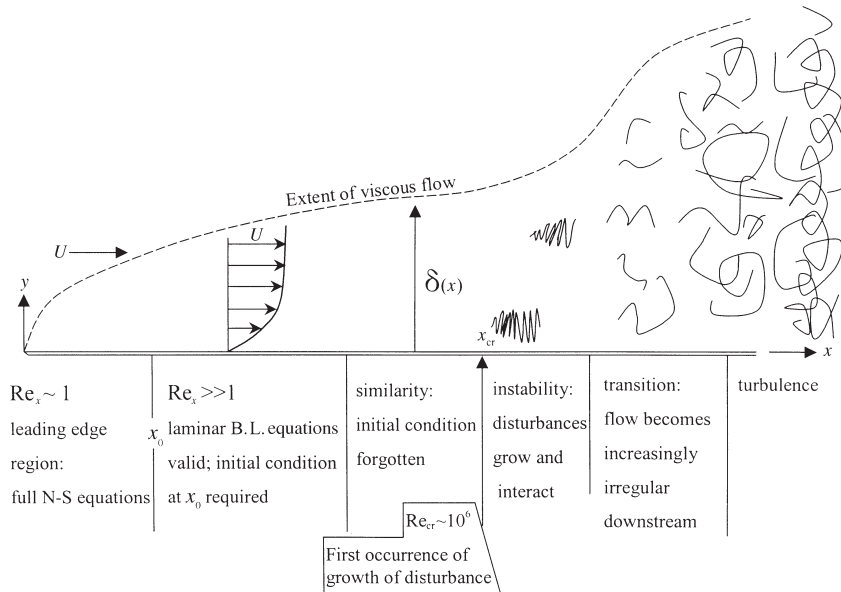

FIGURE 9.10 Schematic depiction of flow over a semi-infinite flat plate. Here, increasing x is synonymous with increasing Reynolds number.

equivalent laminar boundary layer, and a fully turbulent boundary-layer velocity profile has a different shape and different parametric dependencies than an equivalent laminar one. For example, the thickness of a zero-pressure-gradient turbulent boundary layer grows faster than $x^{1/2}$ (Figure 9.10), and the wall shear stress increases faster with U than in a laminar boundary layer where $\tau_0 \propto U^{3/2}$. This increase in friction occurs because turbulent fluctuations produce more wall-normal transport of momentum than that possible from steady viscous diffusion alone. However, both types of boundary layers respond similarly to pressure gradients but with different sensitivities.

Figure 9.11 sketches the nature of the observed variation of the drag coefficient in a flow over a flat plate, as a function of the Reynolds number. The lower curve applies if the boundary layer is laminar over the entire length of the plate, and the upper curve applies if the boundary layer is turbulent over the entire length. The curve joining the two applies to a boundary layer that is laminar over the initial part of the plate, begins transition at $Re_L \sim 5 \times 10^5$, and is fully turbulent for $Re_L > 10^7$. The exact point at which the observed drag deviates from the wholly laminar behavior depends on flow conditions, flow geometry, and surface conditions.

Although surface pressure gradients do affect transition, it may be argued that their most important influence is on boundary-layer separation. A fundamental discussion of boundary-layer separation begins with the steady stream-wise, boundary-layer flow momentum equation, (9.9), where the pressure gradient is found from the external velocity field via (9.11) and with x taken in the stream-wise direction along the surface of interest. At the surface, both velocity components are zero so (9.9) reduces to

$$\mu\left(\frac{\partial^2 u}{\partial y^2}\right)_{wall} = \frac{dp}{dx}.$$
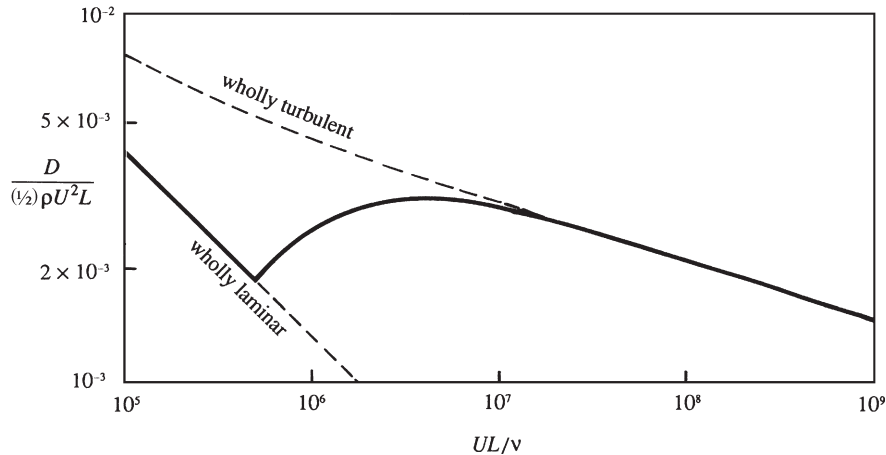

FIGURE 9.11 Measured drag coefficient for a boundary layer over a flat plate. The continuous line shows the drag coefficient for a plate on which the flow is partly laminar and partly turbulent, with the transition taking place at a position where the local Reynolds number is 5×10^5. The dashed lines show the behavior if the boundary layer was either completely laminar or completely turbulent over the entire length of the plate.

In an accelerating stream $dp/dx < 0$, so

$$\left(\frac{\partial^2 u}{\partial y^2}\right)_{wall} < 0 \quad \text{(accelerating)}. \tag{9.51}$$

Given that the velocity profile has to blend smoothly with the external profile, the gradient $\partial u/\partial y$ slightly below the edge of the boundary layer decreases with increasing y from a positive value to zero; therefore, $\partial^2 u/\partial y^2$ slightly below the boundary-layer edge is negative. Equation (9.51) then shows that $\partial^2 u/\partial y^2$ has the same sign at the wall and at the boundary-layer edge, and presumably throughout the boundary layer. In contrast, for a decelerating external stream, $dp/dx > 0$, the curvature of the velocity profile at the wall is

$$\left(\frac{\partial^2 u}{\partial y^2}\right)_{wall} > 0 \quad \text{(decelerating)}, \tag{9.52}$$

so that the profile curvature changes sign somewhere within the boundary layer. In other words, the boundary-layer profile in a decelerating flow has a *point of inflection* where $\partial^2 u/\partial y^2 = 0$, an important fact for boundary-layer stability and transition (see Chapter 11). In the special case of the Blasius boundary layer, the profile's inflection point is at the wall.

The shape of the velocity profiles in Figure 9.12 suggests that a decelerating exterior flow tends to increase the thickness of the boundary layer. This can also be seen from the continuity equation:

$$v(y) = -\int_0^y (\partial u/\partial x)dy.$$

Compared to flow over a flat plate, a decelerating external stream causes a larger $-(\partial u/\partial x)$ within the boundary layer because the deceleration of the outer flow adds to the viscous
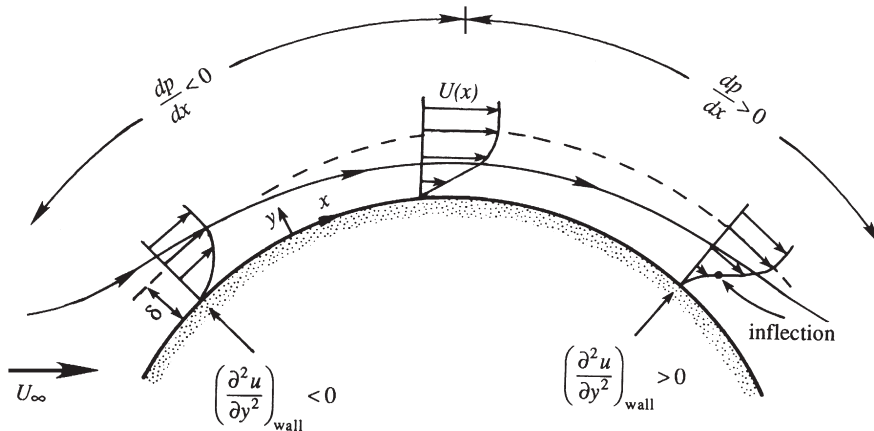

FIGURE 9.12   Velocity profiles across boundary layers with favorable ($dp/dx < 0$) and adverse ($dp/dx > 0$) pressure gradients, as indicated above the flow. The surface shear stress and stream-wise fluid velocity near the surface are highest and lowest in the favorable and adverse pressure gradients, respectively, with the $dp/dx = 0$ case falling between these limits.

deceleration within the boundary layer. It follows from the foregoing equation that the v-field, directed away from the surface, is larger for a decelerating flow. The boundary layer therefore thickens not only by viscous diffusion but also by advection away from the surface, resulting in a more rapid increase in the boundary-layer thickness with x than when the exterior flow is constant or accelerating.

If p falls with increasing x, $dp/dx < 0$, the pressure gradient is said to be *favorable*. If the p rises with increasing x, $dp/dx > 0$, the pressure gradient is said to be *adverse*. In an adverse pressure gradient, the boundary-layer flow decelerates, thickens, and develops a point of inflection. When the adverse pressure gradient is strong enough or acts over a long enough distance, the flow next to the wall reverses direction (Figure 9.13). The point S at which the reverse flow meets the forward flow is a local stagnation point and is known as the *separation point*. Fluid elements approach S (from either side) and are then transported away from the wall. Thus, a separation streamline emerges from the surface at S. Furthermore, the surface shear stress changes sign across S because the surface flow changes direction. Thus, the surface shear stress at S is zero, which implies

$$\left(\frac{\partial u}{\partial y}\right)_{wall} = 0 \quad \text{(separation)}.$$

Once a boundary layer separates from the surface on which it has formed, the surface displacement effect produced by divergence of the body contour and the separation stream-line may be enormous. Additionally, at high Reynolds numbers, a separated boundary layer commonly acquires the properties of a vortex sheet and may rapidly become unstable and transition to a thick zone of turbulence. Thus, boundary-layer separation typically requires the presumed geometry-based, inner-outer and rotational-irrotational flow dichotomies to be reconsidered or even abandoned. In such cases, recourse to experiments or multidimensional numerical solutions may be the only choices for flow investigation.

At Reynolds numbers that are not too large, flow separation may not lead to unsteadiness. For flow past a circular cylinder for $4 < \text{Re} < 40$ the reversed flow downstream of a separation point may form part of a steady vortex behind the cylinder (see Figure 9.16 in Section 9.8). At
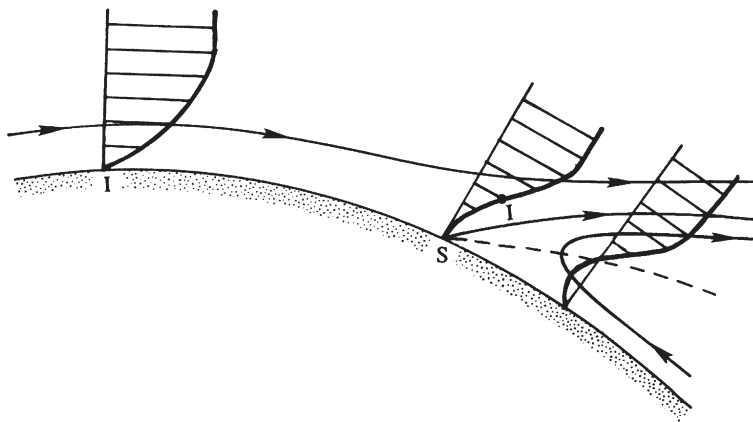

FIGURE 9.13 Streamlines and velocity profiles near a separation point S where a streamline emerges from the surface. The usual boundary-layer equations are not valid downstream of S. The inflection point in the stream-wise velocity profile is indicated by I. The dashed line is the locus of $u = 0$.

higher Reynolds numbers, when the flow on the upstream side of the cylinder develops genuine boundary-layer characteristics, the flow downstream of separation is unsteady and frequently turbulent.

The adverse-pressure gradient strength that a boundary layer can withstand without separating depends on the geometry of the flow and whether the boundary layer is laminar or turbulent. However, a severe adverse-pressure gradient, such as that behind a blunt body, invariably leads to a separation. In contrast, the boundary layer on the trailing surface of a slender body may overcome the weak pressure gradients involved. Therefore, to avoid separation and the resulting form drag penalty, the trailing section of a submerged body should be *gradually* reduced in size, giving it a *streamlined* (or teardrop) shape.

Experimental evidence indicates that the point of separation is relatively insensitive to the Reynolds number as long as the boundary layer is laminar. However, a *transition to turbulence delays boundary-layer separation*; that is, a turbulent boundary layer is more capable of withstanding an adverse pressure gradient. This is because the velocity profile in a turbulent boundary layer places more high-speed fluid near the surface (Figure 9.14). For example, the laminar boundary layer over a circular cylinder separates at ~82° from the forward stagnation point, whereas a turbulent layer over the same body separates at 125° (shown later in Figure 9.16). Experiments show that the surface pressure remains fairly uniform downstream of separation and has a lower value than the pressures on the forward face of the body. The resulting drag due to such fore-aft pressure differences is called *form drag*, as it depends crucially on the shape of the body (and the location of boundary-layer separation). For a blunt body like a sphere, the form drag is larger than the skin friction drag because of the occurrence of separation. For a streamlined body like a rowing shell for crew races, skin friction is generally larger than the form drag. As long as the separation point is located at the same place on the body, the drag coefficient of a blunt body is nearly constant at high Reynolds numbers. However, the drag coefficient drops suddenly when the boundary layer
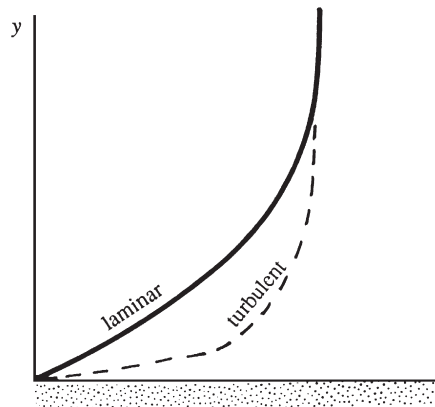

FIGURE 9.14   Nominal comparison of laminar and mean-turbulent, stream-wise velocity profiles in a boundary layer. Here the primary differences are the presence of higher speed fluid closer to the surface and greater surface shear stress in the turbulent layer.
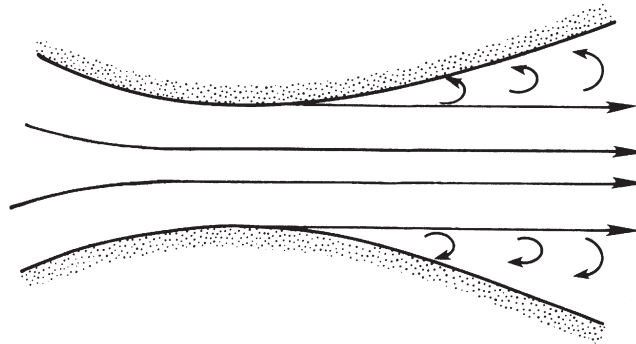
FIGURE 9.15   Separation of flow in a divergent channel. Here, an adverse pressure gradient has led to boundary-layer separation just downstream of the narrowest part of the channel. Such separated flows are instable and are exceedingly likely to be unsteady, even if all the boundary conditions are time independent.

undergoes transition to turbulence, the separation point moves aft, and the body's wake becomes narrower (see Figure 9.21 in Section 9.8).

Boundary-layer separation may take place in internal as well as external flows. An example is a divergent channel or diffuser (Example 9.2, Figure 9.15). Downstream of a narrow point in a ducted flow, an adverse-pressure gradient can cause separation. Elbows, tees, and valves in pipes and tubes commonly lead to regions of internal flow separation, too.

Again it must be emphasized that the boundary-layer equations are valid only as far downstream as the point of separation, if it is known. Beyond separation, the basic underlying assumptions of boundary-layer theory become invalid. Moreover, the parabolic character of the boundary-layer equations requires that a numerical integration is possible only in the direction of advection (along which information is propagated). In a region of reversed flow, this integration direction is *upstream*. Thus, a forward (downstream) integration of the boundary-layer equations breaks down after separation. Furthermore, potential theory may not be used to determine the pressure in a separated flow region, since the flow there is rotational and the effective boundary between irrotational and rotational flow regions is no longer the solid surface but some unknown shape encompassing part of the body's contour, the separation streamline, and, possibly, a wake-zone contour.

9.8. FLOW PAST A CIRCULAR CYLINDER

In general, analytical solutions of viscous flows can be found (possibly in terms of perturbation series) only in two limiting cases, namely Re ≪ 1 and Re ≫ 1. In the Re ≪ 1 limit the inertia forces are negligible over most of the flow field; the Stokes-Oseen solutions discussed in the preceding chapter are of this type. In the opposite limit of Re ≫ 1, the viscous forces are negligible everywhere except close to the surface, and a solution may be attempted by matching an irrotational outer flow with a boundary layer near the surface. In the intermediate range of Reynolds numbers, finding analytical solutions becomes almost an impossible task, and one has to depend on experimentation and numerical solutions. Some of these

experimental flow patterns are described in this section, taking the flow over a circular cylinder as an example. Instead of discussing only the intermediate Reynolds number range, we shall describe the experimental data for the entire range from small to very high Reynolds numbers.

Low Reynolds Numbers

Consider creeping flow around a circular cylinder, characterized by $\text{Re} = U_\infty d/\nu < 1$, where U_∞ is the upstream flow speed and d is the cylinder's diameter. Vorticity is generated close to the surface because of the no-slip boundary condition. In the Stokes approximation this vorticity is simply diffused, not advected, which results in a fore and aft symmetry. The Oseen approximation partially takes into account the advection of vorticity, and results in an asymmetric velocity distribution *far* from the body (which was shown in Figure 8.20). The vorticity distribution is qualitatively analogous to the dye distribution caused by a source of colored fluid at the position of the body. The color diffuses symmetrically in very slow flows, but at higher flow speeds the dye is confined behind a parabolic boundary with the dye source at the parabola's focus.

For increasing Re above unity, the Oseen approximation breaks down, and the vorticity is increasingly confined behind the cylinder because of advection. For $\text{Re} > 4$, two small steady eddies appear behind the cylinder and form a closed separation zone contained with a separation streamline. This zone is sometimes called a *separation bubble*. The cylinder's wake is completely laminar and the vortices rotate in a manner that is consistent with the exterior flow (Figure 9.16). These eddies grow in length and width as Re increases.

Moderate Reynolds Numbers

A very interesting sequence of events begins to develop when Re reaches 40, the point at which the wake behind the cylinder becomes unstable. Experiments show that for $\text{Re} \sim 10^2$ the wake develops a slow oscillation in which the velocity is periodic in time and downstream distance, with the amplitude of the oscillation increasing downstream. The oscillating wake rolls up into two staggered rows of vortices with opposite sense of rotation (Figure 9.17). Von Karman investigated the phenomenon as a problem of superposition of irrotational vortices; he concluded that a nonstaggered row of vortices is unstable, and a staggered row is stable only if the ratio of lateral distance between the vortices to their longitudinal distance is 0.28. Because of the similarity of the wake with footprints in a street, the staggered row of vortices behind a blunt body is called a *von Karman vortex street*. The vortices move downstream at a speed smaller than U_∞. This means that the vortex pattern slowly follows the cylinder if it is pulled through a stationary fluid.

In the range $40 < \text{Re} < 80$, the vortex street does not interact with the pair of attached vortices. As Re increases above 80, the vortex street forms closer to the cylinder, and the attached eddies (whose downstream length has now grown to be about twice the diameter of the cylinder) themselves begin to oscillate. Finally the attached eddies periodically break off alternately from the two sides of the cylinder. While an eddy on one side is shed, that on the other side forms, resulting in an unsteady flow near the cylinder. As vortices of opposite circulations are shed off alternately from the two sides, the circulation around the cylinder
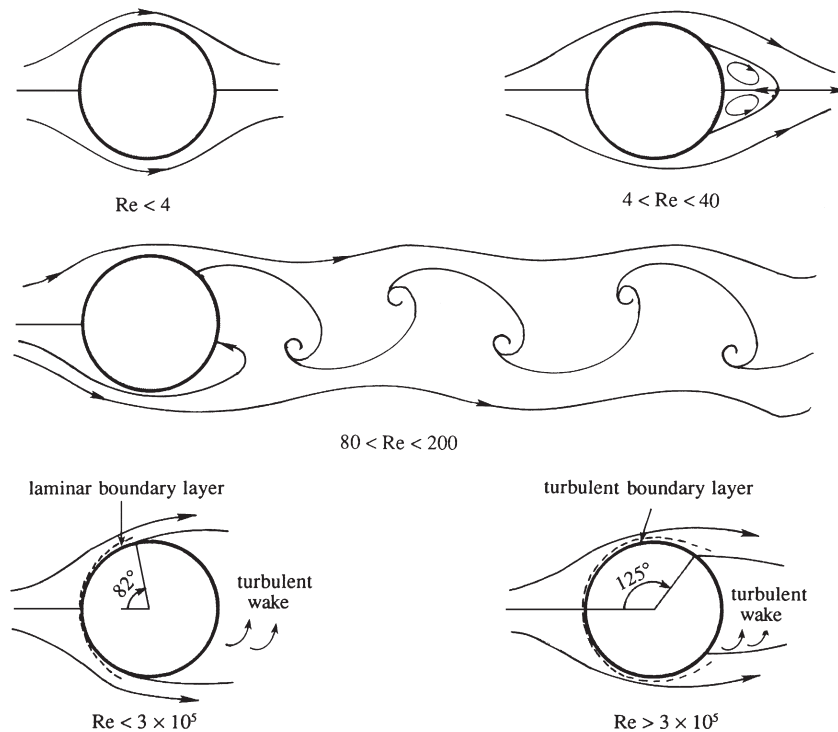
FIGURE 9.16   Depiction of some of the flow regimes for a circular cylinder in a steady uniform cross flow. Here $Re = U_\infty d/\nu$ is the Reynolds number based on free-stream speed U_∞ and cylinder diameter d. At the lowest Re, the streamlines approach perfect fore-aft symmetry. As Re increases, asymmetry increases and steady wake vortices form. With further increase in Re, the wake becomes unsteady and forms the alternating-vortex von Karman vortex street. For Re up to $Re_{cr} \sim 3 \times 10^5$, the laminar boundary layer separates approximately $82°$ from the forward separation point. Above this Re value, the boundary-layer transitions to turbulence, and separation is delayed to $125°$ from the forward separation point.
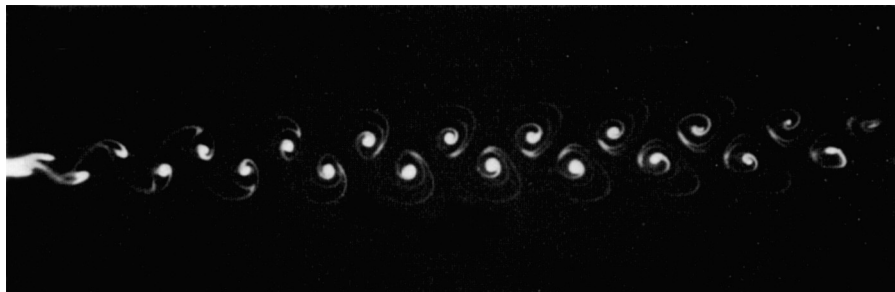

FIGURE 9.17   Von Karman vortex street downstream of a circular cylinder at $Re = 55$. *Flow visualized by condensed milk. S. Taneda,* Jour. Phys. Soc., Japan **20**: *1714–1721, 1965, and reprinted with the permission of The Physical Society of Japan and Dr. Sadatoshi Taneda.*
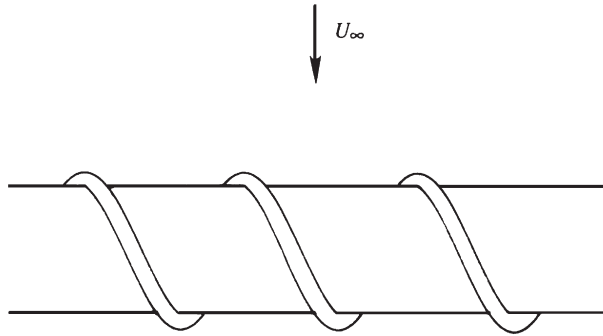
FIGURE 9.18   Spiral blades used for breaking up the span-wise coherence of vortex shedding from a cylindrical rod. Coherent vortex shedding can produce tonal noise and potentially large (and undesired) structural loads on engineered devices that encounter wind or water currents.

changes sign, resulting in an oscillating lift or lateral force perpendicular to the upstream flow direction. If the frequency of vortex shedding is close to the natural frequency of some structural mode of vibration of the cylinder and its supports, then an appreciable lateral vibration may be observed. Engineered structures such as suspension bridges, oil drilling platforms, and even automobile components are designed to prevent coherent shedding of vortices from cylindrical structures. This is done by including spiral blades protruding out of the cylinder's surface, which break up the span-wise coherence of vortex shedding, forcing the vortices to detach at different times along the length of these structures (Figure 9.18).

The passage of regular vortices causes velocity measurements in the cylinder's wake to have a dominant periodicity, and this frequency Ω is commonly expressed as a *Strouhal number* (4.102), $St = \Omega d / U_\infty$. Experiments show that for a circular cylinder the value of S remains close to 0.2 for a large range of Reynolds numbers. For small values of cylinder diameter and moderate values of U_∞, the resulting frequencies of the vortex shedding and oscillating lift lie in the acoustic range. For example, at $U_\infty = 10$ m/s and a wire diameter of 2 mm, the frequency corresponding to a Strouhal number of 0.2 is $n = 1000$ cycles per second. The *singing* of telephone and electrical transmission lines and automobile radio antennae have been attributed to this phenomenon. The value of the *St* given here is that observed in three-dimensional flows with nominally two-dimensional boundary conditions. Moving soap-film experiments and calculations suggest a somewhat higher value of $St = 0.24$ in perfectly two-dimensional flow (see Wen & Lin, 2001).

Below Re = 200, the vortices in the wake are laminar and continue to be so for very large distances downstream. Above 200, the vortex street becomes unstable and irregular, and the flow within the vortices themselves becomes chaotic. However, the flow in the wake continues to have a strong frequency component corresponding to a Strouhal number of $S = 0.2$. However, above a Reynolds number of several thousand, periodicity in the wake is only perceptible near the cylinder, and the wake may be described as fully turbulent beyond several cylinder diameters downstream.

Striking examples of vortex streets have also been observed in stratified atmospheric flows. Figure 9.19 shows a satellite photograph of the wake behind several isolated mountain
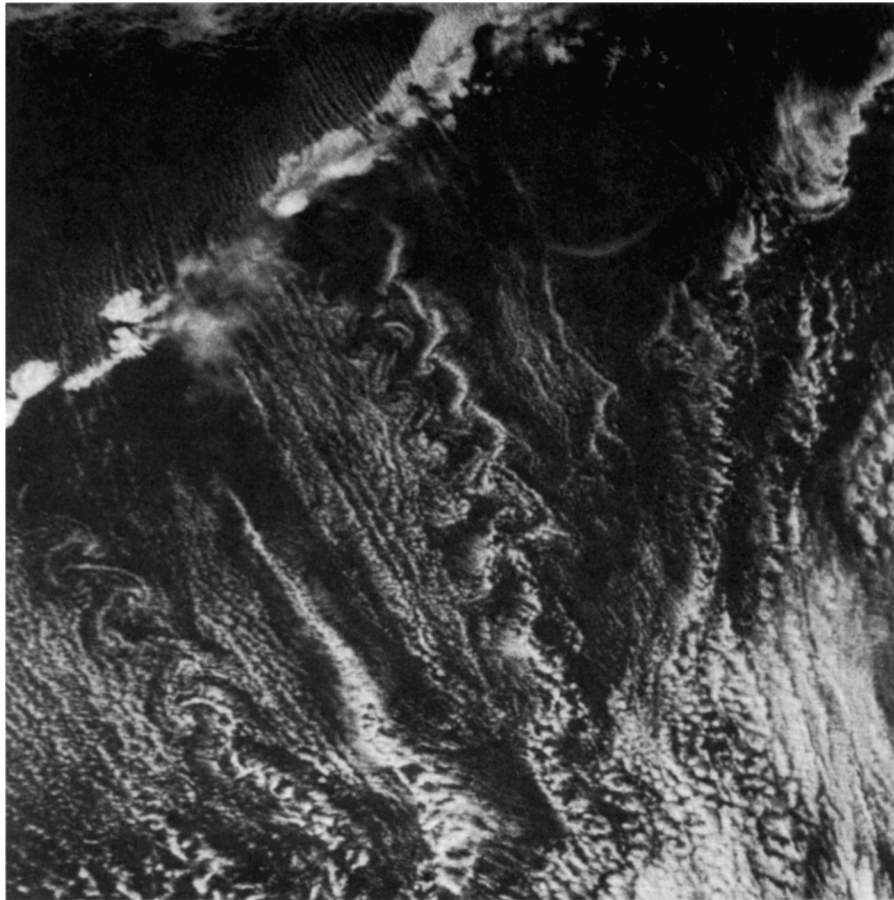
FIGURE 9.19   A von Karman vortex street downstream of mountain peaks in a strongly stratified atmosphere. There are several mountain peaks along the linear, light-colored feature running diagonally in the upper left-hand corner of the photograph. North is upward, and the wind is blowing toward the southeast. *R. E. Thomson and J. F. R. Gower,* Monthly Weather Review *105: 873—884, 1977; reprinted with the permission of the American Meteorological Society.*

peaks through which the wind is blowing toward the southeast. The mountains pierce through the cloud level, and the flow pattern becomes visible by the cloud pattern. The wakes behind at least two mountain peaks display the characteristics of a von Karman vortex street. The strong density stratification in this flow has prevented vertical motions, giving the flow the two-dimensional character necessary for the formation of vortex streets.

High Reynolds Numbers

At high Reynolds numbers the frictional effects upstream of separation are confined near the surface of the cylinder, and the boundary-layer approximation is valid as far downstream

FIGURE 9.20 Surface pressure distribution around a circular cylinder at subcritical and super-critical Reynolds numbers. Note that the pressure is nearly constant within the wake and that the wake is narrower for flow at supercritical Re. The change in the top- and bottom-side, boundary-layer separation points near Re_{cr} is responsible for the change in C_p shown.
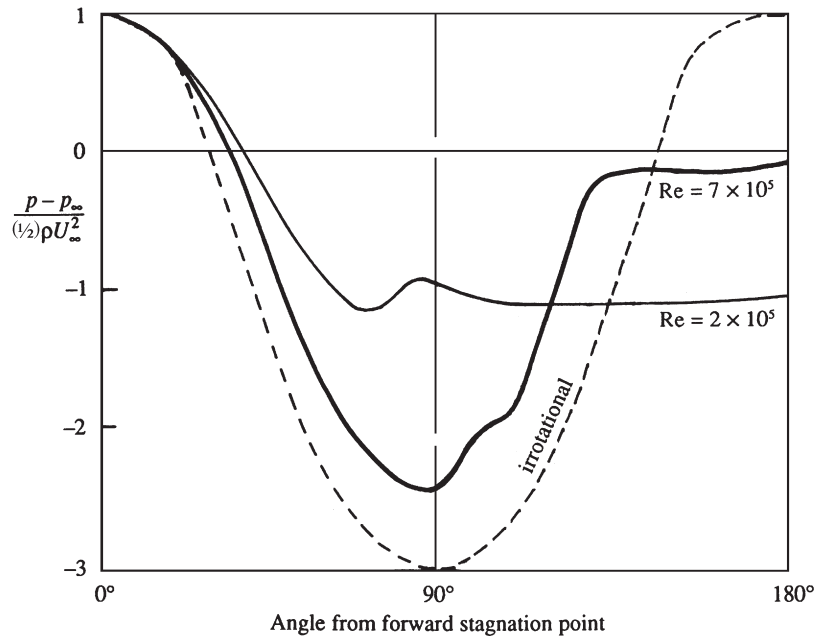
as the point of separation. For a smooth cylinder up to $Re < 3 \times 10^5$, the boundary layer remains laminar, although the wake formed behind the cylinder may be completely turbulent. The laminar boundary layer separates at $\approx 82°$ from the forward stagnation point (Figure 9.16). The pressure in the wake downstream of the point of separation is nearly constant and lower than the upstream pressure (Figure 9.20). The drag on the cylinder in this Re range is primarily due to the asymmetry in the pressure distribution caused by boundary-layer separation, and, since the point of separation remains fairly stationary in this Re range, the cylinder's drag coefficient C_D also stays constant at a value near unity (see Figure 9.21).

Important changes take place beyond the critical Reynolds number of $Re_{cr} \sim 3 \times 10^5$. When $3 \times 10^5 < Re < 3 \times 10^6$, the laminar boundary layer becomes unstable and transitions to turbulence. Because of its greater average near-surface flow speed, a turbulent boundary layer is able to overcome a larger adverse-pressure gradient. In the case of a circular cylinder the turbulent boundary layer separates at $125°$ from the forward stagnation point, resulting in a thinner wake and a pressure distribution more similar to that of potential flow. Figure 9.20 compares the pressure distributions around the cylinder for two values of Re, one with a laminar and the other with a turbulent boundary layer. It is apparent that the pressures within the wake are higher when the boundary layer is turbulent, resulting in a drop in the drag coefficient from 1.2 to 0.33 at the point of transition. For values of $Re > 3 \times 10^6$, the separation point slowly moves upstream as the Reynolds number increases, resulting in a mild increase of the drag coefficient (Figure 9.21).

It should be noted that the critical Reynolds number at which the boundary layer undergoes transition is strongly affected by two factors, namely the intensity of fluctuations
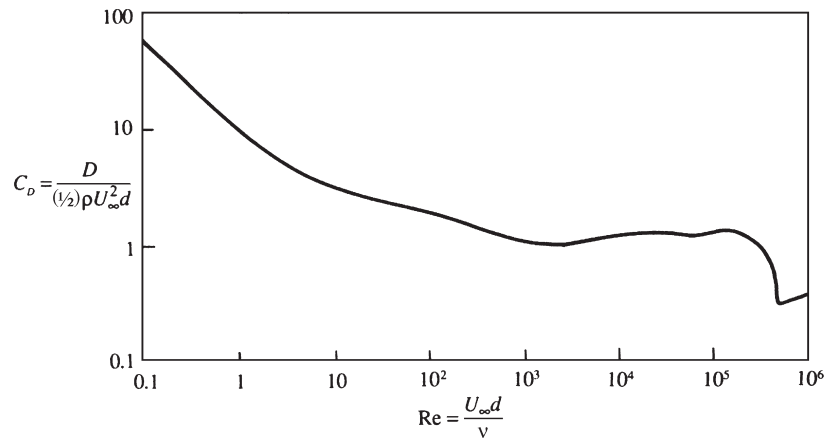
FIGURE 9.21   Measured drag coefficient, C_D, of a smooth circular cylinder vs. $Re = U_\infty d/\nu$. The sharp dip in C_D near Re_{cr} is due to the transition of the boundary layer to turbulence, and the consequent downstream movement of the point of separation and change in the cylinder's surface pressure distribution.

existing in the approaching stream and the roughness of the surface, an increase in either of which decreases Re_{cr}. The value of 3×10^5 is found to be valid for a smooth circular cylinder at low levels of fluctuation of the oncoming stream.

We close this section by noting that this flow illustrates three instances where the solution is counterintuitive. First, small causes can have large effects. If we solve for the flow of a fluid with zero viscosity around a circular cylinder, we obtain the results of Section 6.3. The inviscid flow has fore-aft symmetry and the cylinder experiences zero drag. The bottom two panels of Figure 9.16 illustrate the flow for small viscosity. In the limit as viscosity tends to zero, the flow must look like the last panel in which there is substantial fore-aft asymmetry, a significant wake, and significant drag. This is because of the necessity of a boundary layer and the satisfaction of the no-slip boundary condition on the surface so long as viscosity is not exactly zero. When viscosity is exactly zero, there is no boundary layer and there is slip at the surface. Thus, the resolution of d'Alembert's paradox lies in the existence of, and an understanding of, the boundary layer.

The second instance of counterintuitivity is that symmetric problems can have nonsymmetric solutions. This is evident in the intermediate Reynolds number middle panel of Figure 9.16. Beyond a Reynolds number of ≈ 40, the symmetric wake becomes unstable and a pattern of alternating vortices called a *von Karman vortex street* is established. Yet the equations and boundary conditions are symmetric about a central plane in the flow. If one were to solve only a half problem, assuming symmetry, a solution would be obtained, but it would be unstable to infinitesimal disturbances and unlikely to be observed in a laboratory.

The third instance of counterintuitivity is that there is a range of Reynolds numbers where roughening the surface of the body can reduce its drag. This is true for all blunt bodies. In this range of Reynolds numbers, the boundary layer on the surface of a blunt body is laminar, but sensitive to disturbances such as surface roughness, which would cause earlier transition of the boundary layer to turbulence than would occur on a smooth body. Although the skin

FIGURE 9.22 Measured drag coefficient, C_D, of a smooth sphere vs. $\text{Re} = U_\infty d/\nu$. The Stokes solution is $C_D = 24/\text{Re}$, and the Oseen solution is $C_D = (24/\text{Re}) \quad (1 + 3\text{Re}/16)$; these two solutions are discussed at the end of Chapter 8. The increase of drag coefficient in the range A–B has relevance in explaining why the flight paths of sports balls bend in the air.
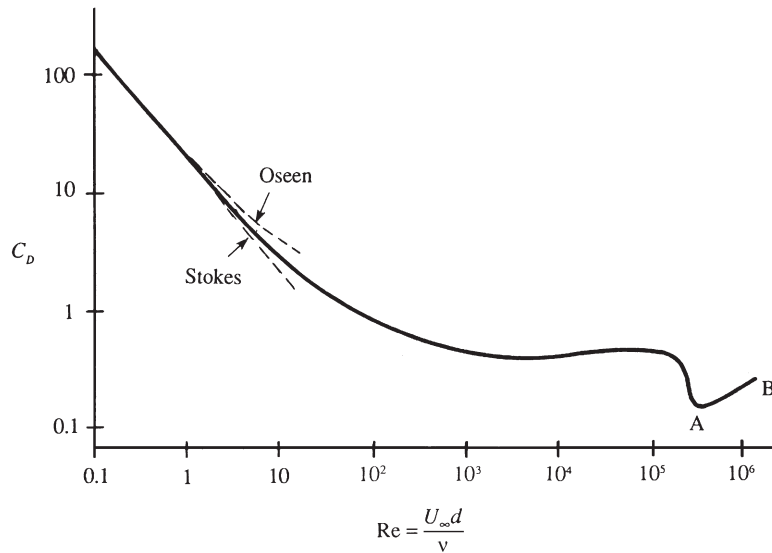
friction of a turbulent boundary layer is much larger than that of a laminar boundary layer, most of the drag on a bluff body is caused by incomplete pressure recovery on its downstream side as shown in Figure 9.20, rather than by skin friction. In fact, it is because the skin friction of a turbulent boundary layer is much larger—as a result of a larger velocity gradient at the surface—that a turbulent boundary layer can remain attached farther on the downstream side of a blunt body, leading to a narrower wake, more complete pressure recovery, and reduced drag. The drag reduction attributed to the turbulent boundary layer is shown in Figure 9.21 for a circular cylinder and Figure 9.22 for a sphere.

9.9. FLOW PAST A SPHERE AND THE DYNAMICS OF SPORTS BALLS

Several features of the description of flow over a circular cylinder qualitatively apply to flows over other two-dimensional blunt bodies. For example, a vortex street is observed in a flow perpendicular to a finite flat plate. The flow over a three-dimensional body, however, has one fundamental difference in that a regular vortex street is absent. For flow around a sphere at low Reynolds numbers, there is an attached eddy in the form of a doughnut-shaped ring; in fact, an axial section of the flow looks similar to that shown in Figure 9.16 for the range $4 < \text{Re} < 40$. For $\text{Re} > 130$ the ring-eddy oscillates, and some of it breaks off periodically in the form of distorted vortex loops.

The behavior of the boundary layer around a sphere is similar to that around a circular cylinder. In particular it undergoes transition to turbulence at a critical Reynolds number of $\text{Re}_{cr} \sim 5 \times 10^5$, which corresponds to a sudden dip of the drag coefficient (Figure 9.22). As in the case of a circular cylinder, the *separation point slowly moves upstream for postcritical Reynolds numbers*, accompanied by a rise in the drag coefficient. The behavior of the

separation point for flow around a sphere at subcritical and supercritical Reynolds numbers is responsible for the bending in the flight paths of sports balls.

In many sports (tennis, cricket, soccer, ping-pong, baseball, golf, etc.), the trajectory of a moving ball may bend in potentially unexpected ways. Such bending may be known as *curve*, *swing*, *hook*, *swerve*, *slice*, etc. The problem has been investigated by wind-tunnel tests and by stroboscopic photographs of flight paths in field tests, a summary of which was given by Mehta (1985). Evidence indicates that the mechanics of trajectory bending is different for spinning and nonspinning balls. The following discussion gives a qualitative explanation of the mechanics of sports-ball trajectory bending. (Readers not interested in sports may omit the rest of this section!)

Cricket Ball Dynamics

A cricket ball has a prominent (1-mm high) seam, and tests show that the orientation of the seam is responsible for the bending of the ball's flight path. It is known to bend when thrown at speeds of around 30 m/s, which is equivalent to a Reynolds number of $Re = U_\infty d/\nu \sim 10^5$, U_∞ is the speed of the ball, and d is its diameter. This Re is somewhat less than the critical value of $Re_{cr} = 5 \times 10^5$ necessary for transition of the boundary layer on a smooth sphere into turbulence. However, the presence of the seam is able to trip the laminar boundary layer into turbulence on one side of the ball (the lower side in Figure 9.23), while the boundary layer on the other side remains laminar. This transition asymmetry leads to boundary-layer separation asymmetry. Typically, the boundary layer on the laminar side separates at $\approx 85°$, whereas that on the turbulent side separates at $120°$. Compared to region B, the surface pressure near region A is therefore closer to that given by the potential flow theory (which predicts a suction pressure of $(p_{min} - p_\infty)/(1/2)\rho U_\infty^2 = -5/4$; see (6.91)). In other words, the pressures are lower on side A, resulting in a downward force on the ball. (Note that Figure 9.23 is a view of the flow pattern looking downward on the ball, so that it corresponds to a ball that bends to the left in its flight. The flight of a cricket ball oriented as in Figure 9.23 is called an *outswinger* in cricket literature, in contrast to an *inswinger* for which the seam is oriented in the opposite direction so as to generate an upward force in Figure 9.23.)
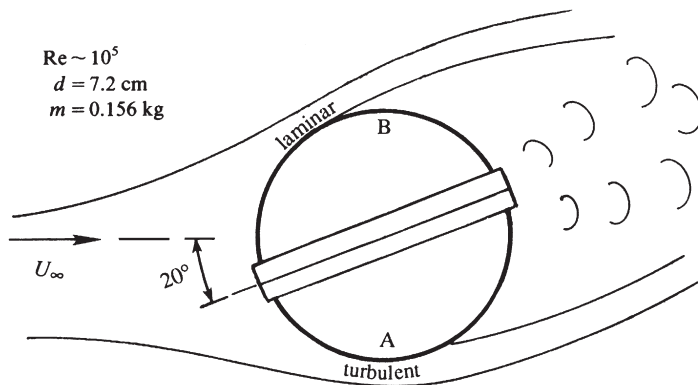

FIGURE 9.23 The swing (or curve) of a cricket ball. The seam is oriented in such a way that a difference in boundary-layer separation points on the top and bottom sides of the ball lead to a downward lateral force in the figure; the surface pressure at A is less than the surface pressure at B.
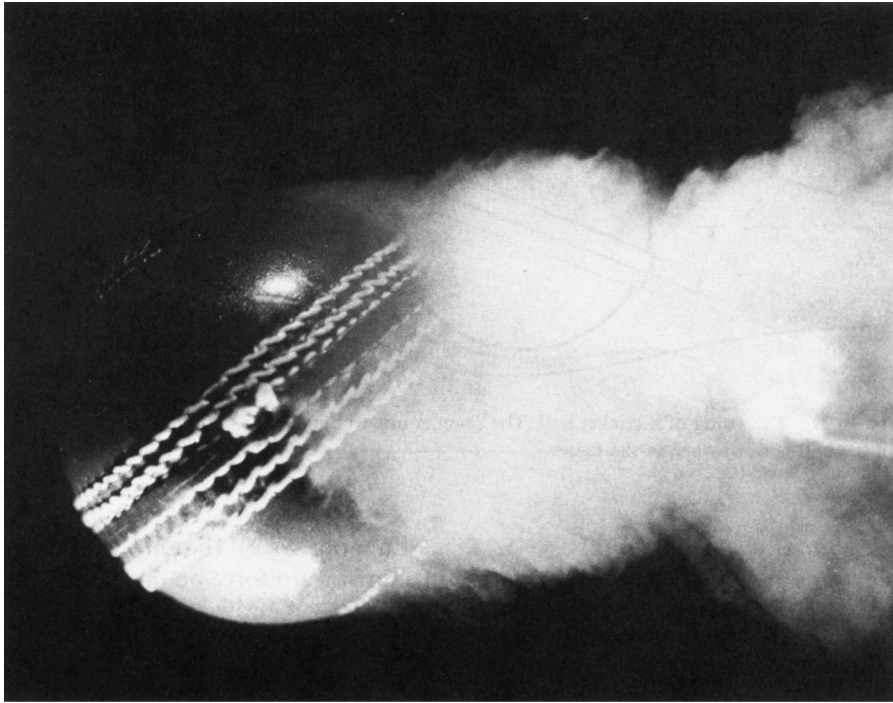
FIGURE 9.24   Smoke photograph of flow over a cricket ball in the same orientation and flow condition as that depicted in Figure 9.23. The flow is from left to right, the seam angle is 40°, the flow speed is 17 m/s, and $Re = 0.85 \times 10^5$. *R. Mehta,* Ann. Rev Fluid Mech. *17: 151−189, 1985. Photograph reproduced with permission from the* Annual Review of Fluid Mechanics, *Vol. 17 © 1985 by* Annual Reviews, www.AnnualReviews.org.

Figure 9.24, a photograph of a cricket ball in a wind-tunnel experiment, clearly shows the delayed separation on the seam side. Note that the wake has been deflected upward by the presence of the ball, implying that an upward force has been exerted by the ball on the fluid. It follows that a downward force has been exerted by the fluid on the ball.

In practice some spin is invariably imparted to the ball. The ball is held along the seam and, because of the round arm action of the bowler, some backspin is always imparted *along* the seam. This has the important effect of stabilizing the orientation of the ball and preventing it from wobbling. A typical cricket ball can generate side forces amounting to almost 40% of its weight. A constant lateral force oriented in the same direction causes a deflection proportional to the square of time. The ball therefore travels in a parabolic path that can bend as much as 0.8 m by the time it reaches the batsman.

It is known that the trajectory of the cricket ball does not bend if the ball is thrown too slow or too fast. In the former case even the presence of the seam is not enough to trip the boundary layer into turbulence, and in the latter case the boundary layer on both sides could be turbulent; in both cases an asymmetric flow is prevented. It is also clear why only a new, shiny ball is able to swing, because the rough surface of an old ball causes the boundary layer to become turbulent on both sides. Fast bowlers in cricket maintain one

hemisphere of the ball in a smooth state by constant polishing. It therefore seems that most of the known facts about the swing of a cricket ball have been adequately explained by scientific research. The feature that has not been explained is the universally observed fact that a cricket ball swings more in humid conditions. The changes in density and viscosity due to changes in humidity can change the Reynolds number by only 2%, which cannot explain this phenomenon.

Tennis Ball Dynamics

Unlike the cricket ball, the path of the tennis ball bends because of spin. A ball hit with topspin curves downward, whereas a ball hit with underspin (backspin) travels in a much flatter trajectory. The direction of the lateral force is therefore in the same sense as that of the Magnus effect experienced by a circular cylinder in potential flow with circulation (see Section 6.3). The mechanics, however, are different. The potential flow argument (involving the Bernoulli equation) offered to account for the lateral force around a circular cylinder cannot explain why a *negative* Magnus effect is universally observed at lower Reynolds numbers. (By a negative Magnus effect we mean a lateral force opposite to that experienced by a cylinder with a circulation of the same sense as the rotation of the sphere.) The correct argument seems to be the asymmetric boundary-layer separation caused by the spin. In fact, the phenomenon was not properly explained until the boundary-layer concepts were understood in the twentieth century. Some pioneering experimental work on the bending paths of spinning spheres was conducted by Robins (1742) over two hundred years ago; the deflection of rotating spheres is sometimes called the *Robins effect*.

Experimental data on nonrotating spheres (Figure 9.22) shows that the boundary layer on a sphere undergoes transition at $Re_{cr} = 5 \times 10^5$, as indicated by a sudden drop in the drag coefficient. This drop is due to the transition of the laminar boundary layer to turbulence. An important point for the present discussion is that for supercritical Reynolds numbers the separation point slowly moves upstream, as evidenced by the increase of the drag coefficient after the sudden drop shown in Figure 9.22.

With this background, we are now in a position to understand how a spinning ball generates a negative Magnus effect at $Re < Re_{cr}$ and a positive Magnus effect at $Re < Re_{cr}$. For a clockwise rotation of the ball, the fluid velocity *relative to the surface* is larger on the lower side (Figure 9.25). For the lower Reynolds number case (Figure 9.25a), this causes a transition of the boundary layer on the lower side, while the boundary layer on the upper side remains laminar. The result is a delayed separation and lower pressure on the bottom surface, and a consequent downward force on the ball. The force here is in a sense opposite to that of the Magnus effect.

The rough surface of a tennis ball lowers the critical Reynolds number, so that for a well-hit tennis ball the boundary layers on both sides of the ball have already undergone transition. Due to the higher relative velocity, the flow near the bottom has a higher Reynolds number, and is therefore farther along the Re-axis of Figure 9.22, in the range AB in which the separation point moves upstream with an increase of the Reynolds number. The separation therefore occurs *earlier* on the bottom side, resulting in a higher pressure there than on the top. This causes an upward lift force and a positive Magnus effect. Figure 9.25b shows that a tennis ball hit with underspin (backspin) generates an upward force; this overcomes

FIGURE 9.25 Curving flight of rotating spheres, in which F indicates the force exerted by the fluid: (a) negative Magnus effect; and (b) positive Magnus effect. A well-hit tennis ball with spin is likely to display the positive Magnus effect.

(a) Re < Re$_{cr}$ (b) Re > Re$_{cr}$
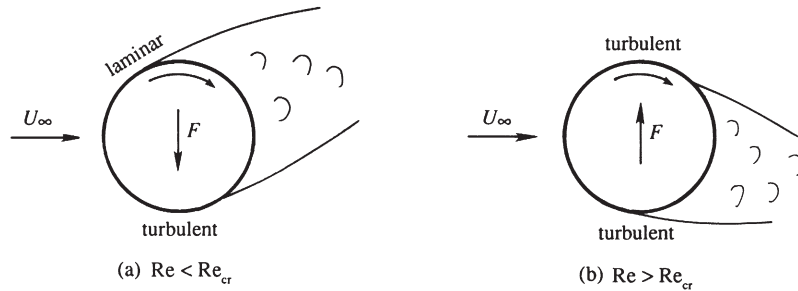
a large fraction of the weight of the ball, resulting in a much flatter trajectory than that of a tennis ball hit with topspin. A *slice serve*, in which the ball is hit tangentially on the right-hand side, curves to the left due to the same effect. Presumably soccer balls curve in the air due to similar dynamics.

Baseball Dynamics

A baseball pitcher uses different kinds of deliveries, a typical Reynolds number being 1.5×10^5. One type of delivery is called a *curveball*, caused by sidespin imparted by the pitcher to bend away from the side of the throwing arm. A *screwball* has the opposite spin and oppositely curved trajectory, when thrown correctly. The dynamics are similar to that of a spinning tennis ball (Figure 9.25b). Figure 9.26 is a photograph of the flow over a spinning baseball, showing an asymmetric separation, a crowding together of streamlines at the bottom, and an upward deflection of the wake that corresponds to a downward force on the ball.

The *knuckleball*, on the other hand, is released without any spin. In this case the path of the ball bends due to an asymmetric separation caused by the orientation of the seam, much like the cricket ball. However, the cricket ball is released with spin along the seam, which stabilizes the orientation and results in a predictable bending. The knuckleball, on the other hand, tumbles in its flight because of a lack of stabilizing spin, resulting in an irregular orientation of the seam and a consequent irregular trajectory.

9.10. TWO-DIMENSIONAL JETS

The previous nine sections have considered boundary layers over solid surfaces. The concept of a boundary layer, however, is more general, and the approximations involved are applicable whenever the vorticity in the flow is confined in thin layers, even in the absence of a solid surface. Such a layer can be in the form of a jet of fluid ejected from an orifice, a wake (where the velocity is lower than the upstream velocity) behind a solid object, or a thin shear layer (vortex sheet) between two uniform streams of different speeds. As an illustration of the method of analysis of these *free shear flows*, we shall consider the case of a laminar two-dimensional jet, which is an efflux of fluid from a long and narrow orifice that issues into a large quiescent reservoir of the same fluid. Downstream from the orifice,
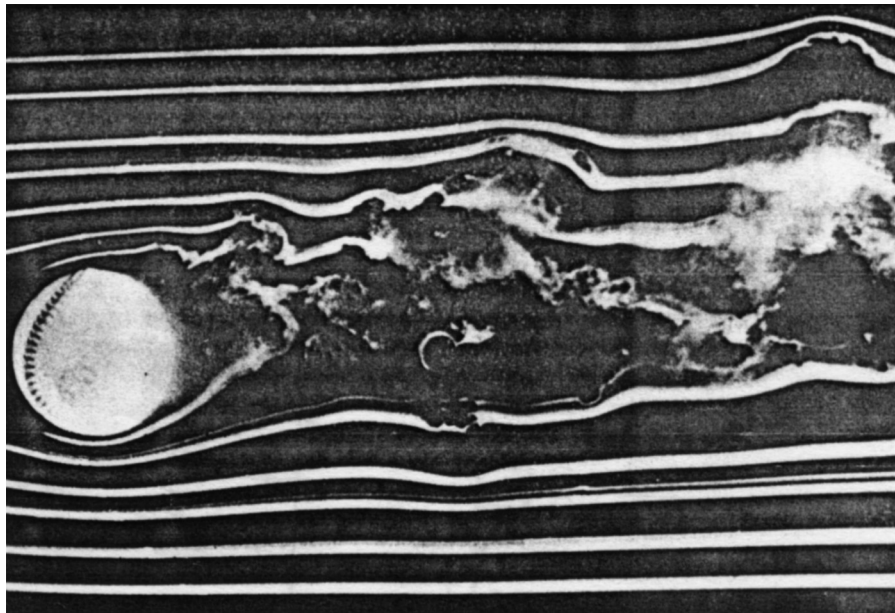
FIGURE 9.26   Smoke photograph of flow around a spinning baseball. Flow is from left to right, flow speed is 21 m/s, and the ball is spinning counterclockwise at 15 rev/s. *[Photograph by F. N. M. Brown, University of Notre Dame.] Photograph reproduced with permission from the* Annual Review of Fluid Mechanics, *Vol. 17 © 1985 by* Annual Reviews, www.AnnualReviews.org.

some of the ambient fluid is carried along with the moving jet fluid through viscous vorticity diffusion at the outer edge of the jet (Figure 9.27). The process of drawing reservoir fluid into the jet by is called *entrainment*.

The velocity distribution near the opening of the jet depends on the details of conditions upstream of the orifice exit. However, because of the absence of an externally imposed length
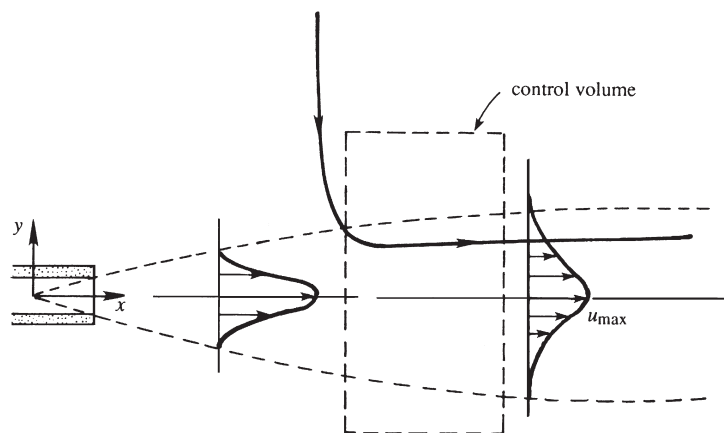

FIGURE 9.27 Simple laminar two-dimensional free jet. A narrow slot injects fluid horizontally with an initial momentum flux J into a nominally quiescent reservoir of the same fluid. The region of horizontally moving fluid slows and expands as x increases. A typical streamline showing entrainment of surrounding fluid is indicated.

scale in the downstream direction, the velocity profile in the jet approaches a self-similar shape not far from where it emerges into the reservoir, regardless of the velocity distribution at the orifice.

For large Reynolds numbers, the jet is narrow and the boundary-layer approximation can be applied. Consider a control volume with sides cutting across the jet axis at two sections (Figure 9.27); the other two sides of the control volume are taken at large distances from the jet axis. No external pressure gradient is maintained in the surrounding fluid so dp/dx is zero. According to the boundary-layer approximation, the same zero pressure gradient is also impressed upon the jet. There is, therefore, no net force acting on the surfaces of the control volume, and this requires the x-momentum flux at the two sections across the jet to be the same.

Let $u_0(x)$ be the stream-wise velocity on the x-axis and assume $\mathrm{Re} = u_0 x/\nu$ is sufficiently large for the boundary-layer equations to be valid. The flow is steady, two-dimensional (x, y), without body forces, and with constant properties (ρ, μ). Then $\partial/\partial y \gg \partial/\partial x$, $v \ll u$, $\partial p/\partial y = 0$, so the fluid equations of motion are the same as for the Blasius boundary layer: (6.2) and (9.18). However, the boundary conditions are different here:

$$u = 0 \quad \text{for } y \to \pm \infty \text{ and } x > 0, \tag{9.53}$$

$$v = 0 \quad \text{on } y = 0 \quad \text{for } x > 0, \text{ and} \tag{9.54}$$

$$u = \tilde{u}(y) \quad \text{on } x = x_0, \tag{9.55}$$

where $\tilde{u}$ is a (known) flow profile. Now partially follow the derivation of the von Karman boundary-layer integral equation. Multiply (6.2) by u and add it to the left side of (9.18) but this time integrate over all y to find:

$$\int_{-\infty}^{+\infty} 2u\frac{\partial u}{\partial x}dy + \int_{-\infty}^{+\infty} \left[u\frac{\partial v}{\partial y} + v\frac{\partial u}{\partial y}\right]dy = \int_{-\infty}^{+\infty} \frac{\partial \tau}{\partial y}dy, \quad \text{or} \quad \frac{d}{dx}\int_{-\infty}^{+\infty} u^2 dy + [uv]_{-\infty}^{+\infty} = [\tau]_{-\infty}^{+\infty}. \tag{9.56}$$

Since $u(y = \pm\infty) = 0$, all derivatives of u with respect to y must also be zero at $y = \pm\infty$. Thus, since $\tau = \mu(\partial u/\partial y)$, the second and third terms in the second equation of (9.56) are both zero. Hence, (9.56) reduces to

$$\frac{d}{dx}\int_{-\infty}^{+\infty} u^2 dy = 0, \tag{9.57}$$

a statement that the stream-wise momentum flux is conserved. Thus, when integrated, (9.57) becomes:

$$\int_{-\infty}^{+\infty} u^2 dy = const. = \int_{-\infty}^{+\infty} \tilde{u}^2(y)dy = J/\rho, \tag{9.58}$$

where the second equality follows from (9.55). Here, the constant is the momentum flux in the jet per unit span, J, divided by the fluid density, ρ.

A similarity solution is obtained far enough downstream so that the boundary-layer equations are valid and $\tilde{u}(y)$ has been forgotten. Thus, we can seek a solution in the form of (8.32) or (9.19):

$$\psi = u_0(x)\delta(x)f(\eta), \quad \text{where } \eta = y/\delta(x), \quad \delta(x) = [vx/u_0(x)]^{1/2}, \tag{9.59}$$

and $u_0(x)$ is the stream-wise velocity on $y = 0$. The stream-wise velocity throughout the field is obtained from differentiation:

$$u = \partial\psi/\partial y = [vxu_0(x)]^{1/2}(df/d\eta)[vx/u_0(x)]^{-1/2} = u_0(x)(df/d\eta). \tag{9.60}$$

The final equality here implies that $f' = 1$ on $\eta = 0$. When (9.60) is substituted into (9.58), the dependence of $u_0(x)$ on x is determined:

$$\frac{J}{\rho} = \int\limits_{-\infty}^{+\infty} u^2 dy = u_0^2(x) \int\limits_{-\infty}^{+\infty} f'^2(\eta)dy = u_0^2(x)\delta(x) \int\limits_{-\infty}^{+\infty} f'^2(\eta)d\eta. \tag{9.61}$$

Since the integral is a dimensionless constant $(= C)$, we must have

$$Cu_0^2(x)\delta(x) = Cu_0^{3/2}(x)\cdot(vx)^{1/2} = J/\rho,$$

so

$$u_0(x) = \left[J^2/C^2\rho^2vx\right]^{1/3}, \quad \text{and} \quad \delta(x) = \left[C\rho v^2 x^2/J\right]^{1/3}. \tag{9.62, 9.63}$$

Thus, (9.59) becomes

$$\psi = [Jvx/C\rho]^{1/3}f(\eta) \quad \text{where } \eta = y/\left[C\rho v^2 x^2/J\right]^{1/3}. \tag{9.64}$$

In terms of the stream function, (9.18) becomes:

$$\frac{\partial\psi}{\partial y}\frac{\partial}{\partial x}\left(\frac{\partial\psi}{\partial y}\right) - \frac{\partial\psi}{\partial x}\frac{\partial}{\partial y}\left(\frac{\partial\psi}{\partial y}\right) = v\frac{\partial^2}{\partial y^2}\left(\frac{\partial\psi}{\partial y}\right). \tag{9.65}$$

Evaluating the derivatives using (9.64) and simplifying produces a differential equation for f:

$$3f''' + f''f + f'^2 = 0.$$

The boundary conditions for $x > 0$ are:

$$f' = 0 \quad \text{for} \quad \eta \to \pm\infty, \tag{9.66}$$

$$f' = 1 \quad \text{on } \eta = 0, \text{ and} \tag{9.67}$$

$$f = 0 \quad \text{on } \eta = 0. \tag{9.68}$$

Integrating the differential equation for f once produces:

$$3f'' + f'f = C_1.$$

Evaluating at $\eta = \pm\infty$ implies $C_1 = 0$ from (9.66) since $f' = 0$ implies $f'' = 0$ too. Integrating again yields:

$$3f' + f^2/2 = C_2. \tag{9.69}$$

Evaluating on $\eta = 0$ implies $C_2 = 3$ from (9.67) and (9.68). The independent and dependent variables in (9.69) can be separated and integrated:

$$3\frac{df}{d\eta} = 3 - \frac{f^2}{2} \quad \text{or} \quad \int \frac{df}{1 - f^2/6} = \int d\eta.$$

The integral on the left in the second equality can be evaluated via the variable substitution $f = \sqrt{6} \tanh \beta$, and leads to:

$$\tanh^{-1}\left(\frac{f}{\sqrt{6}}\right) = \frac{\eta}{\sqrt{6}} + C_3, \quad \text{or} \quad f = \sqrt{6} \tanh\left(\frac{\eta}{\sqrt{6}} + C_3\right). \tag{9.70}$$

Evaluating the final expression on $\eta = 0$ implies $C_3 = 0$ from (9.68). Thus, using (9.60), (9.62), and (9.70), the stream-wise velocity field is

$$u(x, y) = u_0(x)f'(\eta) = \left(\frac{J^2}{C^2\rho^2\nu x}\right)^{1/3} \text{sech}^2\left(\frac{y}{\sqrt{6}}\left[\frac{J}{C\rho\nu^2 x^2}\right]^{1/3}\right), \tag{9.71}$$

and the dimensionless constant, C, is determined from

$$C = \int_{-\infty}^{+\infty} f'^2(\eta) \, d\eta = \int_{-\infty}^{+\infty} \text{sech}^4\left(\frac{\eta}{\sqrt{6}}\right) d\eta = \frac{4\sqrt{6}}{3}. \tag{9.72}$$

The mass flux of the jet per unit span is:

$$\dot{m} = \int_{-\infty}^{+\infty} \rho u_0(x)f'(\eta)dy = \rho u_0(x)\delta(x) \int_{-\infty}^{+\infty} f'(\eta)d\eta = \rho u_0(x)\delta(x)[f]_{-\infty}^{+\infty} = \rho u_0(x)\delta(x) \cdot 2\sqrt{6}.$$

Using (9.62), (9.63), and (9.72), this simplifies to:

$$\dot{m} = \left(36J\rho^2\nu x\right)^{1/3}, \tag{9.73}$$

which shows that the jet's mass flux increases with increasing downstream distance as the jet entrains ambient reservoir fluid via the action of viscosity. The jet's entrainment induces flow toward the jet within the reservoir. The vertical velocity is:

$$v = -\frac{\partial\psi}{\partial x} = -\frac{1}{3}\left(\frac{J\nu}{C\rho x^2}\right)^{1/3}[f - 2\eta f'] , \quad \text{or} \quad \frac{v}{u_0(x)} = -\frac{[f - 2\eta f']}{3\sqrt{\text{Re}_x}} \quad \text{where } \text{Re}_x = \frac{xu_0(x)}{\nu}. \tag{9.74}$$

Here, $f(\eta) \to \pm\sqrt{6}$ and $2\eta f'(\eta) = 2\eta\text{sech}^2(\eta/\sqrt{6}) \to 0$ as $\eta \to \pm\infty$, so

$$\frac{v}{u_0(x)} \to \mp\frac{\sqrt{6}}{3\sqrt{\text{Re}_x}} \quad \text{as } \eta \to \pm\infty. \tag{9.75}$$

Thus, the jet's entrainment field is a flow of reservoir fluid toward the jet from above and below.

The jet spreads as it travels downstream, and this can be deduced from (9.71). Following the definition of δ_{99} in Section 9.2, the 99% half width of the jet, h_{99}, may be defined as the y-location where the horizontal velocity falls to 1% of its value at $y = 0$. Thus, from (9.71) we can determine:

$$\text{sech}^2\left(\frac{h_{99}}{\sqrt{6}}\left[\frac{J}{C\rho\nu^2 x^2}\right]^{1/3}\right) = 0.01 \to \frac{h_{99}}{\sqrt{6}}\left[\frac{J}{C\rho\nu^2 x^2}\right]^{1/3} \cong 2.2924 \to h_{99} \cong 5.6152\left[\frac{C\rho\nu^2 x^2}{J}\right]^{1/3},$$

$$(9.76)$$

which shows the jet width grows with increasing downstream distance like $x^{2/3}$. Viscosity increases the jet's thickness but higher momentum jets are thinner. The Reynolds numbers based on the stream-wise (x) and cross-stream (h_{99}) dimensions of the jet are:

$$\text{Re}_x = \frac{xu_0(x)}{\nu} = \left(\frac{3Jx}{4\sqrt{6}\rho\nu^2}\right)^{2/3} \quad \text{and} \quad \text{Re}_{h_{99}} = \frac{h_{99}u_0(x)}{\nu} = 5.6152\left(\frac{3Jx}{4\sqrt{6}\rho\nu^2}\right)^{1/3}.$$

Unfortunately, this steady-flow, two-dimensional laminar jet solution is not readily observable because the flow is unstable when $\text{Re} \gg 1$. The low critical Reynolds number for instability of a jet or wake is associated with the existence of one or more inflection points in the stream-wise velocity profile, as discussed in Chapter 11. Nevertheless, the laminar solution has revealed at least two significant phenomena—constancy of jet momentum flux and increase of jet mass flux through entrainment—that also apply to round jets and turbulent jets. However, the cross-stream spreading rate of a turbulent jet is found to be independent of Reynolds number and is faster than the laminar jet, being more like $h_{99} \propto x$ rather than $h_{99} \propto x^{2/3}$ (see Chapter 13).

A second example of a two-dimensional jet that also shares some boundary-layer characteristics is the *wall jet*. The solution here is due to Glauert (1956). We consider fluid exiting a narrow slot with its lower boundary being a planar wall taken along the x-axis (see Figure 9.28). Near the wall ($y = 0$) the flow behaves like a boundary layer, but far from the wall it behaves like a free jet. For large Re_x the jet is thin ($\delta/x \ll 1$) so $\partial p/\partial y \approx 0$ across it. The pressure is constant in the nearly stagnant outer fluid so $p \approx$ const. throughout the flow. Here again the fluid mechanical equations of motion are (6.2) and (9.18). This time the boundary conditions are:

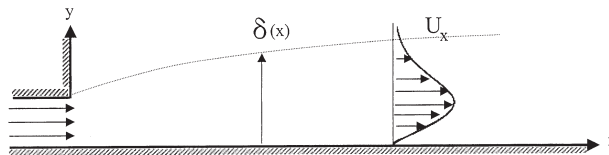$$u = v = 0 \quad \text{on } y = 0 \quad \text{for } x > 0, \text{ and} \tag{9.77}$$

FIGURE 9.28   The laminar two-dimensional wall jet. A narrow slot injects fluid horizontally along a smooth flat wall. As for the free jet, the thickness of the region of horizontally moving fluid slows and expands as x increases but with different dependencies.

$$u(x, y) \to 0 \quad \text{as } y \to \infty. \tag{9.78}$$

Here again, a similarity solution valid for $\text{Re}_x \to \infty$ can be found under the assumption that the initial velocity distribution is forgotten by the flow. However, unlike the free jet, the momentum flux of the wall jet is not constant; it diminishes with increasing downstream distance because of the wall shear stress. To obtain the conserved property in the wall jet, integrate (9.18) from y to ∞:

$$\int_y^\infty u \frac{\partial u}{\partial x} dy + \int_y^\infty v \frac{\partial u}{\partial y} \, dy = \nu \int_y^\infty \frac{\partial^2 u}{\partial y^2} \, dy = \nu \left[\frac{\partial u}{\partial y} \right]_y^\infty = -\nu \frac{\partial u}{\partial y},$$

multiply this by u, and integrate from 0 to ∞:

$$\int_0^\infty \left(u \frac{\partial}{\partial x} \int_y^\infty \frac{u^2}{2} dy \right) dy + \int_0^\infty \left(u \int_y^\infty v \frac{\partial u}{\partial y} dy \right) dy = -\frac{\nu}{2} \int_0^\infty \frac{\partial u^2}{\partial y} \, dy = -\frac{\nu}{2} [u^2]_0^\infty = 0.$$

The final equality follows from the boundary conditions (9.77) and (9.78). Integrating the interior integral of the second term on the left by parts and using (6.2) yields a term equal to the first term and one that lacks any differentiation:

$$\int_0^\infty \left(u \frac{\partial}{\partial x} \int_y^\infty u^2 dy \right) dy - \int_0^\infty u^2 v dy = 0. \tag{9.79}$$

Now consider

$$\frac{d}{dx} \int_0^\infty \left(u \int_y^\infty u^2 \, dy \right) dy = \int_0^\infty \left(\frac{\partial u}{\partial x} \int_y^\infty u^2 \, dy \right) dy + \int_0^\infty \left(u \frac{\partial}{\partial x} \int_y^\infty u^2 \, dy \right) dy,$$

use (6.2) in the first term on the right side, integrate by parts, and combine this with (9.79) to obtain

$$\frac{d}{dx} \int_0^\infty \left(u \int_y^\infty u^2 dy \right) dy = 0. \tag{9.80}$$

This says that the flux of exterior momentum flux remains constant with increasing downstream distance and is the necessary condition for obtaining similarity exponents.

As for the steady free laminar jet, the field equation is (9.65) and the solution is presumed to be in the similarity form specified by (9.59). Here $u_0(x)$ is to be determined and this similarity solution should be valid when $x \gg x_o$, where x_o is the location where the initial condition is specified, which we take to be the upstream extent of the validity of the

boundary-layer momentum equation (9.18) or (9.65). Substituting $u = \partial\psi/\partial y = u_0(x)f'(\eta)$ from (9.59) into (9.80) produces:

$$\frac{d}{dx}\left[u_0^3(x) \cdot \frac{\nu x}{u_0(x)}\int_0^\infty\left(f'\int_\eta^\infty f'^2 d\eta\right)d\eta\right] = 0. \tag{9.81}$$

If the double integration is independent of x, then the factor outside the integral must be constant. Therefore, set $xu_0^2(x) = C^2$, which implies $u_0(x) = Cx^{-1/2}$ so (9.59) becomes:

$$\psi(x, y) = \left[\nu Cx^{1/2}\right]^{1/2}f(\eta) \quad \text{where } \eta = y/\delta(x), \ \delta(x) = \left[\nu x^{3/2}/C\right]^{1/2}. \tag{9.82}$$

After appropriately differentiating (9.82), substituting into (9.65), and canceling common factors, (9.65) reduces to

$$f''' + ff'' + 2f'^2 = 0,$$

subject to the boundary conditions (9.77) and (9.78): $f(0) = 0; f'(0) = 0; f'(\infty) = 0$. This third-order equation can be integrated once after multiplying by the integrating factor f, to yield $4ff'' - 2f'^2 + f^2f' = 0$, where the constant of integration has been evaluated at $\eta = 0$. Dividing by the integrating factor $4f^{3/2}$ allows another integration. The result is

$$f^{-1/2}f' + f^{3/2}/6 = C_1 \equiv f_\infty^{3/2}/6, \quad \text{where } f_\infty = f(\infty).$$

The final integration can be performed by separating variables and defining $g^2(\eta) = f/f_\infty$:

$$\int\frac{df}{f_\infty^{3/2}f - f^2} = \frac{1}{6}\int d\eta, \quad \text{or} \quad \int\frac{dg}{1 - g^3} = \frac{f_\infty}{12}\int d\eta.$$

The integration on the left may be performed via a partial fraction expansion using $1 - g^3 = (1 - g) \cdot (1 + g + g^2)$ with the final result in left-implicit form:

$$-\ln(1 - g) + \sqrt{3}\tan^{-1}\left(\frac{2g + 1}{\sqrt{3}}\right) + \ln\left(1 + g + g^2\right)^{1/2} = \frac{f_\infty}{4}\eta + \sqrt{3}\tan^{-1}\left(\frac{1}{\sqrt{3}}\right), \tag{9.83}$$

where the boundary condition $g(0) = 0$ was used to evaluate the constant of integration. The profiles of f and f' are plotted vs. η in Figure 9.29. We can verify easily that $f \to 0$ exponentially fast in η from this solution for $g(\eta)$. As $\eta \to \infty$, $g \to 1$, so for large η the solution for g reduces to $-\ln(1 - g) + \sqrt{3}\tan^{-1}\sqrt{3} + (1/2)ln3 \cong f_\infty\eta/4 + \sqrt{3}\tan^{-1}(1/\sqrt{3})$. The first term on each side of this equation dominates, leaving $1 - g \approx e^{-(f_\infty/4)\eta}$. Thus, for $\eta \to \infty$, we must have: $f' = 2f_\infty gg' \approx \frac{1}{2}f_\infty^2\exp[-f_\infty\eta/4]$. The mass flow rate per unit span in the steady laminar wall jet is

$$\dot{m} = \int_0^\infty \rho u dy = \rho u_0(x)\delta(x)\int_0^\infty f'(\eta)d\eta = \rho\sqrt{\nu C}f_\infty x^{1/4}, \tag{9.84}$$

FIGURE 9.29 Variation of normalized mass flux (f) and normalized stream-wise velocity profile (f') with similarly variable η for the laminar two-dimensional wall jet. *Reprinted with the permission of Cambridge University Press.*
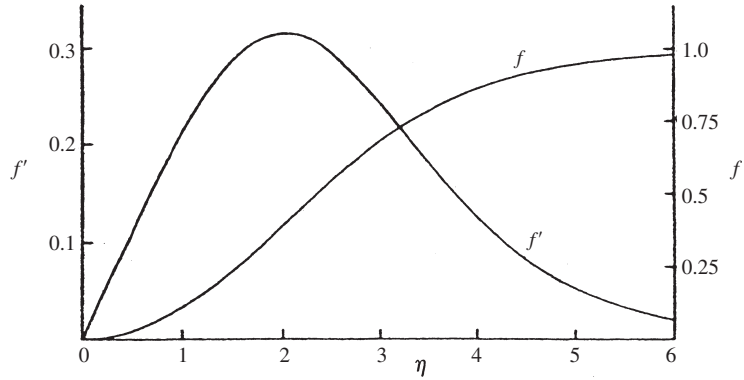
indicating that entrainment increases the mass flow rate in the jet with $x^{1/4}$. The two constants, C and f_∞, can be determined from the integrated form of (9.81) in terms of Ψ, the flux of the exterior momentum flux (a constant):

$$u_0^2(x)\nu x \int_0^\infty \left(f' \int_\eta^\infty f'^2 d\eta \right) d\eta = C^2\nu \int_0^\infty \left(f' \int_\eta^\infty f'^2 d\eta \right) d\eta = \Psi, \tag{9.85}$$

and knowledge of $\dot{m}$ at one downstream location.

The entrainment into the steady laminar wall jet is evident from the form of $v = -\partial\psi/\partial x = -\sqrt{\nu C}(f - 3\eta f')/4x^{3/4}$, which simplifies to $v \approx -\sqrt{\nu C}f_\infty/4x^{3/4}$ as $\eta \to \infty$, so, far above the jet, the flow is downward toward the jet.

9.11. SECONDARY FLOWS

Large Reynolds number flows with curved streamlines tend to generate additional velocity components because of the properties of boundary layers. These additional components are commonly called *secondary flows*. An example of such a flow is made dramatically visible by randomly dispersing finely crushed tea leaves into a cup of water, and then stirring vigorously in a circular motion. When the motion has ceased, all of the particles have collected in a mound at the center of the bottom of the cup (see Figure 9.30). An explanation of this phenomenon is given in terms of thin boundary layers. The stirring motion imparts a primary velocity, $u_\varphi(R)$ (see Appendix B.6 for coordinates), large enough for the Reynolds number to be large enough for the boundary layers on the cup's sidewalls and bottom to be thin. The two largest terms in the R-momentum equation are

$$\frac{\partial p}{\partial R} = \frac{\rho u_\varphi^2}{R}.$$

Away from the walls, the flow is inviscid. As the boundary layer on the bottom is thin, boundary-layer theory yields $\partial p/\partial z = 0$ from the axial momentum equation. Thus, the pressure in the bottom boundary layer is the same as for the inviscid flow just outside the
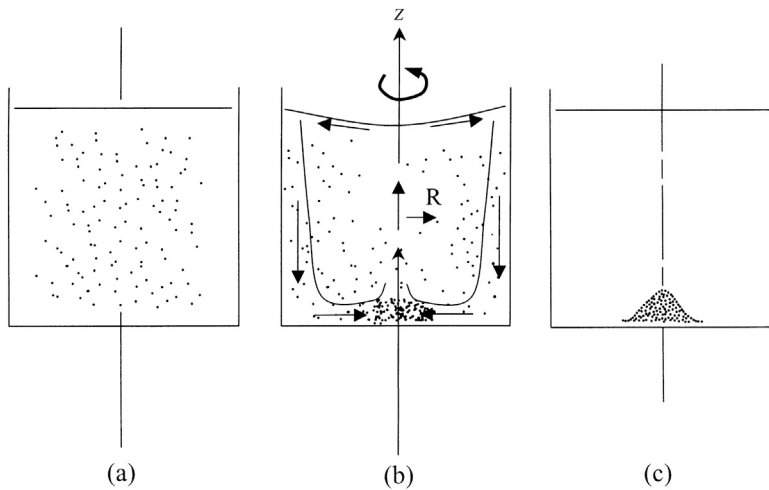
FIGURE 9.30 Secondary flow in a teacup. Tea leaf fragments are slightly denser than water. (a) Tea leaf fragments randomly dispersed—initial state; (b) stirred vigorously—transient motion; and (c) final state where all the tea leaf fragments are piled near the axis of rotation on the bottom of the cup.

boundary layer. However, within the boundary layer, u_ϕ is less than the inviscid value at the edge. Thus $p(R)$ is everywhere larger in the boundary layer than that required for circular streamlines inside the boundary layer, and this pressure difference pushes the streamlines inward toward the center of the cup. That is, the pressure gradient within the boundary layer generates an inwardly directed u_R. This motion induces a downwardly directed flow in the sidewall boundary layer and an outwardly directed flow on the top surface. This secondary flow is closed by an upward flow along the cup's centerline. The visualization is accomplished by crushed tea leaves which are slightly denser than water. They descend by gravity or are driven outward by centrifugal acceleration. If they enter the sidewall boundary layer, they are transported downward and thence to the center by the secondary flow. If the tea particles enter the bottom boundary layer from above, they are quickly swept to the center and dropped as the flow turns upward. All the particles collect at the center of the bottom of the teacup. A practical application of this effect, illustrated in Exercise 9.28, relates to sand and silt transport by the Mississippi River.

EXERCISES

9.1. A thin flat plate 2 m long and 1 m wide is placed at zero angle of attack in a low-speed wind tunnel in the two positions sketched below.
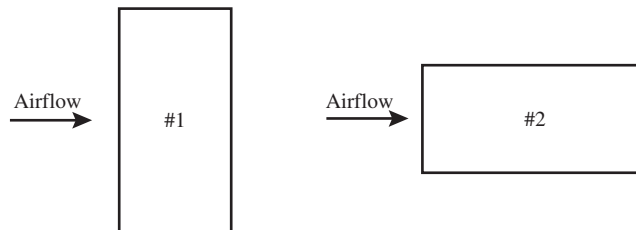
a) For steady airflow, what is the ratio: $\dfrac{\text{drag on the plate in position \#1}}{\text{drag on the plate in position \#2}}$?

b) For steady airflow at 10 m/sec, what is the total drag on the plate in position #1?

c) If the airflow is impulsively raised from zero to 10 m/sec at $t = 0$, will the initial drag on the plate in position #1 be greater or less than the steady-state drag value calculated for part b)?

d) Estimate how long it will take for drag on the plate in position #1 in the impulsively started flow to reach the steady-state drag value calculated for part b)?

9.2. Solve the Blasius equations (9.27) through (9.29) with a computer, using the Runge-Kutta scheme of numerical integration.

9.3. A flat plate 4 m wide and 1 m long (in the direction of flow) is immersed in kerosene at 20°C ($v = 2.29 \times 10^{-6}$ m²/s, $\rho = 800$ kg/m³), flowing with an undisturbed velocity of 0.5 m/s. Verify that the Reynolds number is less than critical everywhere, so that the flow is laminar. Show that the thickness of the boundary layer and the shear stress at the center of the plate are $\delta = 0.74$ cm and $\tau_0 = 0.2$ N/m², and those at the trailing edge are $\delta = 1.05$ cm and $\tau_0 = 0.14$ N/m². Show also that the total frictional drag on one side of the plate is 1.14 N. Assume that the similarity solution holds for the entire plate.

9.4. A simple realization of a temporal boundary layer involves the spinning fluid in a cylindrical container. Consider a viscous incompressible fluid (density $= \rho$, viscosity $= \mu$) in solid body rotation (rotational speed $= \Omega$) in a cylindrical container of diameter d. The mean depth of the fluid is h. An external stirring mechanism forces the fluid to maintain solid body rotation. At $t = 0$, the external stirring ceases. Denote the time for the fluid to spin-down (i.e., to stop rotating) by τ.
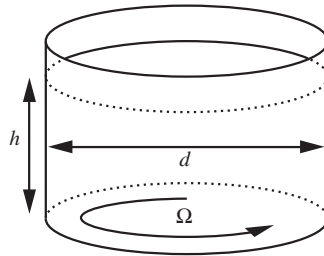

a) For $h \gg d$, write a simple laminar-flow scaling law for τ assuming that the velocity perturbation produced by the no-slip condition on the container's sidewall must travel inward a distance $d/2$ via diffusion.

b) For $h \ll d$, write a simple laminar-flow scaling law for τ assuming that the velocity perturbation produced by the no-slip condition on the container's bottom must travel upward a distance h via diffusion.

c) Using partially filled cylindrical containers of several different sizes (drinking glasses and pots and pans are suggested) with different amounts of water, test the validity of the above diffusion estimates. Use a spoon or a whirling motion of the container to bring the water into something approaching solid body rotation. You'll

know when the fluid motion is close to solid body rotation because the fluid surface will be a paraboloid of revolution. Once you have this initial flow condition set up, cease the stirring or whirling and note how long it takes for the fluid to stop moving. Perform at least one test when d and h are several inches or more. Cookie or bread crumbs sprinkled on the water surface will help visualize surface motion. The judicious addition of a few drops of milk after the fluid starts slowing down may prove interesting.

d) Compute numbers from your scaling laws for parts a) and b) using the viscosity of water, the dimensions of the containers, and the experimental water depths. Are the scaling laws from parts a) and b) useful for predicting the experimental results? If not, explain why.

(The phenomena investigated here have some important practical consequences in atmospheric and oceanic flows and in IC engines where swirl and tumble are exploited to mix the fuel charge and increase combustion speeds.)

9.5. A square-duct wind tunnel of length $L = 1$ m is being designed to operate at room temperature and atmospheric conditions. A uniform airflow at $U = 1$ m/s enters through an opening of $D = 20$ cm. Due to the viscosity of air, it is necessary to design a variable cross-sectional area if a constant velocity is to be maintained in the middle part of the cross-section throughout the wind tunnel.


$U = 1$ m/s

20 cm

$D(x)$

$L = 1$ m
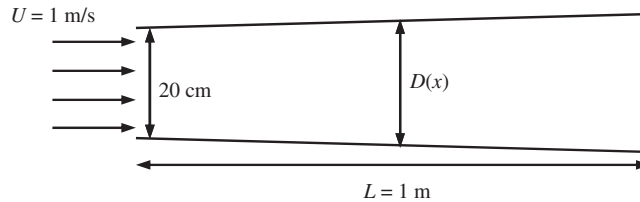
a) Determine the duct size, $D(x)$, as a function of x.
b) How will the result be affected if $U = 20$ m/s? At a given value of x, will $D(x)$ be larger or smaller (or the same) than the value obtained in part a)? Explain.
c) How will the result be affected if the wind tunnel is to be operated at 10 atm (and $U = 1$ m/s)? At a given value of x, will $D(x)$ be larger or smaller (or the same) than the value obtained in part a)? Explain. [*Hint*: the dynamic viscosity of air (μ) is largely unaffected by pressure.]
d) Does the airflow apply a net force to the wind tunnel? If so, indicate the direction of the force.

9.6. Use the control volume shown to derive the definition of the momentum thickness, θ, for flow over a flat plate:

$$\rho U^2 \theta = \rho U^2 \int_0^h \frac{u}{U}\left(1 - \frac{u}{U}\right) dy = \frac{\text{drag force on the plate from zero to } x}{\text{unit depth into the page}} = \int_0^x \tau_0 dx$$

The words in the figure describe the upper and lower control volume boundaries.
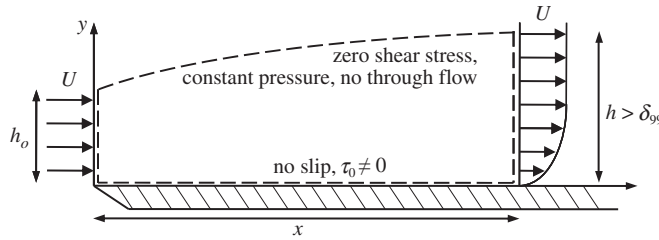
9.7. Estimate the 99% boundary-layer thickness on:
   a) A paper airplane wing (length $= 0.25$ m, $U = 1$ m/sec)
   b) The underside of a super tanker (length $= 300$ m, $U = 5$ m/sec)
   c) An airport runway on a blustery day (length $= 5$ km, $U = 10$ m/sec)
   d) Will these estimates be accurate in each case? Explain.

9.8. Air at 20°C and 100 kPa ($\rho = 1.167$ kg/m^3, $\nu = 1.5 \times 10^{-5}$ m^2/s) flows over a thin plate with a free-stream velocity of 6 m/s. At a point 15 cm from the leading edge, determine the value of y at which $u/U = 0.456$. Also calculate v and $\partial u/\partial y$ at this point. [*Answer:* $y = 0.857$ mm, $v = 0.39$ cm/s, $\partial u/\partial y = 3020$ s^{-1}. You may not be able to achieve this level of accuracy from Figure 9.5 alone.]

9.9. An incompressible fluid (density ρ, viscosity μ) flows steadily from a large reservoir into a long pipe with diameter D. Assume the pipe wall boundary-layer thickness is zero at $x = 0$. The Reynolds number based on D, Re$_D$, is greater than 10^4.
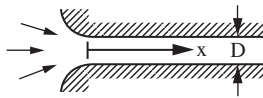
   a) Estimate the necessary pipe length for establishing a parabolic velocity profile in the pipe.
   b) Will the pressure drop in this entry length be larger or smaller than an equivalent pipe length in which the flow has a parabolic profile? Why?

9.10. [1]A variety of different dimensionless groups have been used to characterize the importance of a pressure gradient in boundary layer flows. Develop an expression for each of the following parameters for the Falkner-Skan boundary layer solutions in terms of the exponent n in $U_e(x) = ax^n$, Re$_x = U_e x/\nu$, integrals involving the profile function f', and $f''(0)$, the profile slope at $y = 0$. Here $u(x, y) = U_e(x)f'(y/\delta(x)) = U_e f'(\eta)$ and the wall shear stress $\tau_0 = \mu(\partial u/\partial y)_{y=0} = (\mu U_e/\delta(x))f''(0)$. What value does each parameter take in a Blasius boundary layer? What value does each parameter achieve at the separation condition?
   a) $(\nu/U_e^2)(dU_e/dx)$, an inverse Reynolds number
   b) $(\theta^2/\nu)(dU_e/dx)$, the Holstein and Bohlen correlation parameter

---

[1]Inspired by problem 4.10 on page 330 of White (2006)

c) $(\mu/\sqrt{\rho\tau_0^3})(dp/dx)$, Patel's parameter

d) $(\delta^*/\tau_0)(dp/dx)$, Clauser's parameter

9.11. Consider the boundary layer that develops as a constant density viscous fluid is drawn to a point sink at $x = 0$ on an infinite flat plate in two dimensions (x, y). Here $U_e(x) = -U_oL_o/x$, so set $\eta = y/\sqrt{\nu x/|U_e|}$ and $\psi = -\sqrt{\nu x|U_e|}f(\eta)$ and redo the steps leading to (9.36) to find $f''' - f'^2 + 1 = 0$. Solve this equation and utilize appropriate boundary conditions to find $f' = 3\left[\dfrac{1 - \alpha e^{-\sqrt{2}\eta}}{1 + \alpha e^{-\sqrt{2}\eta}}\right]^2 - 2$

where $\alpha = \dfrac{\sqrt{3} - \sqrt{2}}{\sqrt{3} + \sqrt{2}}$.

9.12. By completing the steps below, show that it is possible to derive von Karman's boundary-layer integral equation without integrating to infinity in the surface-normal direction using the three boundary-layer thicknesses commonly defined for laminar and turbulent boundary layers: 1) δ (or δ_{99}) = the full boundary-layer thickness that encompasses all (or 99%) of the region of viscous influence, 2) δ^* = the displacement thickness of the boundary layer, and 3) θ = momentum thickness of the boundary layer. Here, the definitions of the latter two involve the first:

$\delta^*(x) = \int\limits_{y=0}^{y=\delta}\left(1 - \dfrac{u(x,y)}{U_e(x)}\right)dy$ and $\theta(x) = \int\limits_{y=0}^{y=\delta}\dfrac{u(x,y)}{U_e(x)}\left(1 - \dfrac{u(x,y)}{U_e(x)}\right)dy$, where $U_e(x)$ is the flow speed parallel to the wall outside the boundary layer, and δ is presumed to depend on x too.

a) Integrate the two-dimensional continuity equation from $y = 0$ to δ to show that the vertical velocity at the edge of the boundary layer is: $v(x, y = \delta) = \dfrac{d}{dx}(U_e(x)\delta^*(x)) - \delta\dfrac{dU_e}{dx}$.

b) Integrate the steady two-dimensional x-direction boundary-layer momentum equation from $y = 0$ to δ to show that: $\dfrac{\tau_0}{\rho} = \dfrac{d}{dx}(U_e^2(x)\theta(x)) + \dfrac{\delta^*(x)}{2}\dfrac{dU_e^2(x)}{dx}$.

[*Hint*: Use Leibniz's rule $\dfrac{d}{dx}\int\limits_{a(x)}^{b(x)}f(x,y)dy = \left[f(x,b)\dfrac{db}{dx}\right] - \left[f(x,a)\dfrac{da}{dx}\right] + \int\limits_{a(x)}^{b(x)}\dfrac{\partial f(x,y)}{\partial x}dy$ to handle the fact that $\delta = \delta(x)$.]

9.13. Derive the von Karman boundary layer integral equation by conserving mass and momentum in a control volume (C.V.) of width dx and height h that moves at the exterior flow speed $U_e(x)$ as shown. Here h is a constant distance that is comfortably greater than the overall boundary layer thickness δ.
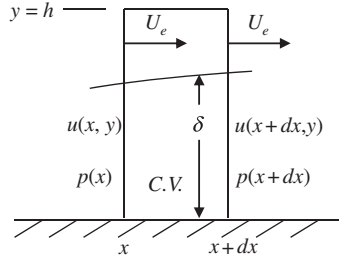
9.14. For the following approximate flat-plate boundary-layer profile:

$$\frac{u}{U} = \left\{ \begin{array}{ll} \sin(\pi y/2\delta) & \text{for } 0 \leq y \leq \delta \\ 1 & \text{for } y > \delta \end{array} \right\},$$

where δ is the generic boundary-layer thickness, determine:
a) The displacement thickness δ^*, the momentum thicknesses θ, and the shape factor $H = \delta^*/\theta$.
b) Use the zero-pressure gradient boundary-layer integral equation to find:
$(\delta/x)Re_x^{1/2}$, $(\delta^*/x)Re_x^{1/2}$, $(\theta/x)Re_x^{1/2}$, $c_f Re_x^{1/2}$, and $C_D Re_L^{1/2}$ for the approximate profile.
c) Compare these results to their equivalent Blasius boundary-layer values.

9.15. An incompressible viscous fluid with kinematic viscosity ν flows steadily in a long two-dimensional horn with cross-sectional area $A(x) = A_o\exp\{\beta x\}$. At $x = 0$, the fluid velocity in the horn is uniform and equal to U_o. The boundary-layer momentum thickness is zero at $x = 0$.
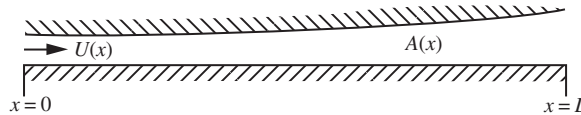

a) Assuming no separation, determine the boundary-layer momentum thickness, $\theta(x)$, on the lower horn boundary using Thwaites' method.
b) Determine the condition on β that makes the no-separation assumption valid for $0 < x < L$.
c) If $\theta(x = 0)$ was nonzero and positive, would the flow in the horn be more or less likely to separate than the $\theta(x = 0) = 0$ case with the same horn geometry?

9.16. The steady two-dimensional velocity potential for a source of strength m located a distance b above a large flat surface located at $y = 0$ is:

$$\phi(x, y) = \frac{m}{2\pi}\left(\ln\sqrt{x^2 + (y - b)^2} + \ln\sqrt{x^2 + (y + b)^2}\right)$$

a) Determine $U(x)$, the horizontal fluid velocity on $y = 0$.

b) Use this $U(x)$ and Thwaites' method to estimate the momentum thickness, $\theta(x)$, of the laminar boundary layer that develops on the flat surface when the initial momentum thickness θ_o is zero. [Potentially useful information:

$$\int_0^x \frac{\xi^5 d\xi}{(\xi^2 + b^2)^5} = \frac{x^6(x^2 + 4b^2)}{24b^4(x^2 + b^2)^4}\Bigg]$$

c) Will boundary-layer separation occur in this flow? If so, at what value of x/b does Thwaites' method predict zero wall shear stress?

d) Using solid lines, sketch the streamlines for the ideal flow specified by the velocity potential given above. For comparison, on the same sketch, indicate with dashed lines the streamlines you expect for the flow of a real fluid in the same geometry at the same flow rate.

9.17. A fluid-mediated particle-deposition process requires a laminar boundary-layer flow with a *constant* shear stress, τ_w, on a smooth flat surface. The fluid has viscosity μ and density ρ (both constant). The flow is steady, incompressible, and two dimensional, and the flat surface extends from $0 < x < L$. The flow speed above the boundary layer is $U(x)$. Ignore body forces.
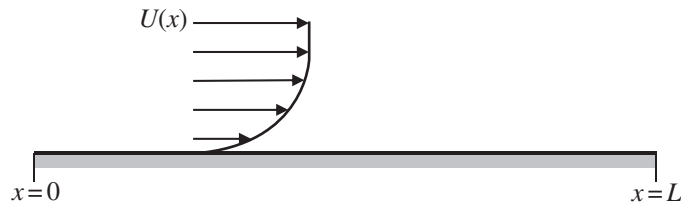
a) Assume the boundary-layer thickness is zero at $x = 0$, and use Thwaites' formulation for the shear stress, $\tau_w = (\mu U/\theta)l(\lambda)$ with $\lambda = (\theta^2/\nu)(dU/dx)$, to determine $\theta(x)$ and $U(x)$ in terms of λ, $\nu = \mu/\rho$, x, and $\tau_w/\mu = $ constant. [*Hint*: assume that $U/\theta = A$ and $l(\lambda)$ are both constants so that $\tau_w/\mu = Al(\lambda)$.]

b) Using the Thwaites integral (9.50) and the results of part a), determine λ.

c) Is boundary-layer separation a concern in this flow? Explain with words or equations.

9.18. The steady two-dimensional potential for incompressible flow at nominal horizontal speed U over a stationary but mildly wavy wall is: $\phi(x, y) = Ux - U\varepsilon \exp(-ky) \cos(kx)$, where $k\varepsilon \ll 1$. Here, ε is the amplitude of the waviness and $k = 2\pi/\lambda$, where λ is the wavelength of the waviness.

a) Use the potential to determine the horizontal velocity $u(x, y)$ on $y = 0$.

b) Assume that $u(x, 0)$ from part a) is the exterior velocity on the wavy wall and use Thwaites' method to approximately determine the momentum thickness, θ, of the

laminar boundary layer that develops on the wavy wall when the fluid viscosity is μ, and $\theta = 0$ at $x = 0$. Keep only the linear terms in $k\varepsilon$ and ε/x to simplify your work.

c) Is the average wall shear stress higher for $\lambda/2 \leq x \leq 3\lambda/4$ or for $3\lambda/4 \leq x \leq \lambda$?

d) Does the boundary layer ever separate when $k\varepsilon = 0.01$?

e) In $0 \leq x \leq \lambda$, determine where the wall pressure is the highest and the lowest.

f) If the wavy surface were actually an air-water interface, would a steady wind tend to increase or decrease water wave amplitudes? Explain.
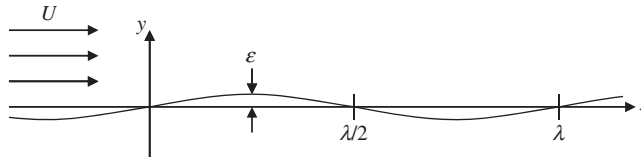

9.19. Consider the boundary layer that develops in stagnation point flow: $U_e(x) = U_o x/L$.

a) With $\theta = 0$ at $x = 0$, use Thwaites' method to determine $\delta^*(x)$, $\theta(x)$, and $c_f(x)$.

b) This flow also has an exact similarity solution of the full Navier-Stokes equations. Numerical evaluation of the final nonlinear ordinary differential equation produces: $c_f \sqrt{Re_x} = 2.4652$, where $Re_x = U_e x/\nu = U_o x^2/L\nu$. Assess the accuracy of the predictions for $c_f(x)$ from the Thwaites' method for this flow.

9.20. A laminar boundary layer develops on a large smooth flat surface under the influence of an exterior flow velocity $U(x)$ that varies with downstream distance, x.

a) Using Thwaites' method, find a single integral-differential equation for $U(x)$ if the boundary layer is to remain perpetually right on the verge of separation so that the wall shear stress, τ_0, is zero. Assume that the boundary layer has zero thickness at $x = 0$.

b) Assume $U(x) = U_o(x/L)^\gamma$ and use the result of part a) to find γ.

c) Compute the boundary-layer momentum thickness $\theta(x)$ for this situation.

d) Determine the extent to which the results of parts b) and c) satisfy the von Karman boundary-layer integral equation, (9.43), when $\tau_0 = 0$ by computing the residual of this equation. Interpret the meaning of your answer; is von Karman's equation well satisfied, or is the residual of sufficient size to be problematic?

e) Can the $U(x)$ determined for part b) be produced in a duct with cross-sectional area $A(x) = A_o(x/L)^{-\gamma}$? Explain your reasoning.

9.21. Consider the boundary layer that develops on a cylinder of radius a in a cross flow.
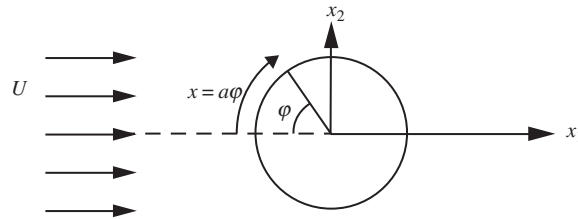
    a) Using Thwaites' method, determine the momentum thickness as a function of φ, the angle from the upstream stagnation point (see drawing).

    b) Make a sketch of c_f versus φ.

    c) At what angle does Thwaites method predict vanishing wall shear stress?

9.22. An incompressible viscous fluid flows steadily in a large duct with constant cross-sectional area A_o and interior perimeter b. A laminar boundary layer develops on the duct's sidewalls. At $x = 0$, the fluid velocity in the duct is uniform and equal to U_o, and the boundary-layer thickness is zero. Assume the thickness of the duct-wall boundary layer is small compared to A_o/b.

    a) Calculate the duct-wall boundary-layer momentum and displacement thicknesses, $\theta(x)$ and $\delta^*(x)$, respectively, using Thwaites' method when $U(x) = U_o$.

    b) Using the $\delta^*(x)$ found for part a), compute a more accurate version of $U(x)$ that includes boundary-layer displacement effects.

    c) Using the $U(x)$ found for part b), recompute $\theta(x)$ and compare to the results of part a). To simplify your work, linearize all the power-law expressions, i.e., $(1 - b\delta^*/A_o)^n \cong 1 - nb\delta^*/A_o$.

    d) If the duct area expanded as the flow moved downstream, would the correction for the presence of the sidewall boundary layers be more likely to move boundary-layer separation upstream or downstream? Explain.

9.23. Water flows over a flat plate 30 m long and 17 m wide with a free-stream velocity of 1 m/s. Verify that the Reynolds number at the end of the plate is larger than the critical value for transition to turbulence. Using the drag coefficient in , estimate the drag on the plate.

9.24. A common means of assessing boundary-layer separation is to observe the surface streaks left by oil or paint drops that were smeared across a surface by the flow. Such investigations can be carried out in an elementary manner for cross-flow past a cylinder using a blow dryer, a cylinder 0.5 to 1 cm in diameter that is ~10 cm long (a common ball-point pen), and a suitable viscous liquid. Here, creamy salad dressing, shampoo, dish washing liquid, or molasses should work. And, for the best observations, the liquid should not be clear and the cylinder and liquid should be different colors. Dip your finger into the viscous liquid and wipe it over two thirds of the surface of the cylinder. The liquid layer should be thick enough so that you can easily tell where it is thick or thin. Use the remaining dry third of the cylinder to hold the cylinder horizontal. Now, turn on the blow dryer, leaving the heat off, and direct its outflow across the wetted

portion of the horizontal cylinder to mimic the flow situation in the drawing for Exercise 9.21.

a) Hold the cylinder stationary, and observe how the viscous fluid moves on the surface of the cylinder and try to determine the angle φ_s at which boundary-layer separation occurs. To get consistent results you may have to experiment with different liquids, different initial liquid thicknesses, different blow-dryer fan settings, and different distances between cylinder and blow dryer. Estimate the cylinder-diameter-based Reynolds number of the flow you've studied.

b) If you have completed Exercise 9.21, do your boundary-layer separation observations match the calculations? Explain any discrepancies between your experiments and the calculations.

9.25. Find the diameter of a parachute required to provide a fall velocity no larger than that caused by jumping from a 2.5 m height, if the total load is 80 kg. Assume that the properties of air are $\rho = 1.167$ kg/m^3, $\nu = 1.5 \times 10^{-5}$ m^2/s, and treat the parachute as a hemispherical shell with $C_D = 2.3$. [*Answer:* 3.9 m]

9.26. Consider incompressible, slightly viscous flow over a semi-infinite flat plate with constant suction. The suction velocity $v(x, y = 0) = v_0 < 0$ is ordered by $O(\text{Re}^{-1/2}) < v_0/U < O(1)$ where $\text{Re} = Ux/\nu \to \infty$. The flow upstream is parallel to the plate with speed U. Solve for u, v in the boundary layer.

9.27. The boundary-layer approximation is sometimes applied to flows that do not have a bounding surface. Here the approximation is based on two conditions: downstream fluid motion dominates over the cross-stream flow, and any moving layer thickness defined in the transverse direction evolves slowly in the downstream direction. Consider a laminar jet of momentum flux J that emerges from a small orifice into a large pool of stationary viscous fluid at $z = 0$. Assume the jet is directed along the positive z-axis in a cylindrical coordinate system. In this case, the steady, incompressible, axisymmetric boundary-layer equations are:

$$\frac{1}{R}\frac{\partial(Ru_R)}{\partial R} + \frac{\partial w}{\partial z} = 0, \quad \text{and} \quad w\frac{\partial w}{\partial z} + u_R\frac{\partial w}{\partial R} = -\frac{1}{\rho}\frac{\partial p}{\partial z} + \frac{\nu}{R}\frac{\partial}{\partial R}\left(R\frac{\partial w}{\partial R}\right),$$

where w is the (axial) z-direction velocity component, and R is the radial coordinate. Let $r(z)$ denote the generic radius of the cone of jet flow.

a) Let $w(R, z) = (\nu/z)f(\eta)$ where $\eta = R/z$, and derive the following equation for f:
$$\eta f' + f \int^{\eta} \eta f d\eta = 0.$$

b) Solve this equation by defining a new function $F = \int^{\eta} \eta f d\eta$. Determine constants from the boundary condition: $w \to 0$ as $\eta \to \infty$, and the requirement:
$$J = 2\pi\rho \int_{R=0}^{R=r(z)} w^2(R, z)R dR = const.$$

c) At fixed z, does $r(z)$ increase or decrease with increasing J?

[*Hints*: 1) The fact that the jet emerges into a pool of quiescent fluid should provide information about $\partial p/\partial z$, and 2) $f(\eta) \propto (1 + const \cdot \eta^2)^{-2}$, but try to obtain this result without using it.]

9.28. Mississippi River boatmen know that when rounding a bend in the river, they must stay close to the outer bank or else they will run aground. Explain in fluid mechanical terms the reason for the cross-sectional shape of the river at the bend.
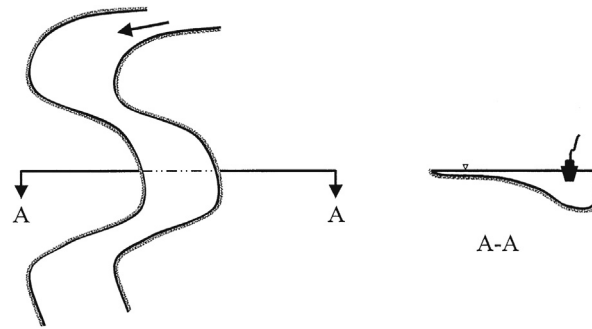
Literature Cited

Batchelor, G. K. (1967). *An Introduction to Fluid Dynamics*. London: Cambridge University Press.

Bender, C. M., & Orszag, S. A. (1978). *Advanced Mathematical Methods for Scientists and Engineers*. New York: McGraw-Hill.

Curle, N. (1962). *The Laminar Boundary Layer Equations*. Oxford: Clarendon Press.

Falkner, V. W., & Skan, S. W. (1931). Solutions of the boundary layer equations. *Phil. Mag. (Ser. 7), 12*, 865−896.

Gallo, W. F., Marvin, J. G., & Gnos, A. V. (1970). Nonsimilar nature of the laminar boundary layer. *AIAA J, 8*, 75−81.

Glauert, M. B. (1956). The Wall Jet. *J. Fluid Mech, 1*, 625−643.

Goldstein, S. (Ed.). (1938). *Modern Developments in Fluid Dynamics*. London: Oxford University Press. Reprinted by Dover, New York (1965).

Holstein, H., & Bohlen, T. (1940). Ein einfaches Verfahren zur Berechnung laminarer Reibungsschichten die dem Näherungsverfahren von K. Pohlhausen genügen. *Lilienthal-Bericht, S10*, 5−16.

Kevorkian, J., & Cole, J. D. (1981). *Perturbation Methods in Applied Mathematics*. New York: Springer-Verlag.

Mehta, R. (1985). Aerodynamics of sports balls. *Annual Review of Fluid Mechanics, 17*, 151−189.

Nayfeh, A. H. (1981). *Introduction to Perturbation Techniques*. New York: Wiley.

Peletier, L. A. (1972). On the asymptotic behavior of velocity profiles in laminar boundary layers. *Arch. for Rat. Mech. and Anal, 45*, 110−119.

Pohlhausen, K. (1921). Zur näherungsweisen Integration der Differentialgleichung der laminaren Grenzschicht. *Z. Angew. Math. Mech, 1*, 252−268.

Robbins, B. (1742). *New Principles of Gunnery: Containing the Determinations of the Force of Gun-powder and Investigations of the Difference in the Resisting Power of the Air to Swift and Slow Motions*. London: J. Nourse.

Schlichting, H. (1979). *Boundary Layer Theory* (7th ed.). New York: McGraw-Hill.

Serrin, J. (1967). Asymptotic behaviour of velocity profiles in the Prandtl boundary layer theory. *Proc. Roy. Soc. A, 299*, 491−507.

Taneda, S. (1965). Experimental investigation of vortex streets. *J. Phys. Soc. Japan, 20*, 1714−1721.

Thomson, R. E., & Gower, J. F. R. (1977). Vortex streets in the wake of the Aleutian Islands. *Monthly Weather Review, 105*, 873−884.

Thwaites, B. (1949). Approximate calculation of the laminar boundary layer. *Aero. Quart, 1*, 245−280.

van Dyke, M. (1975). *Perturbation Methods in Fluid Mechanics*. Stanford, CA: The Parabolic Press.

von Karman, T. (1921). Über laminare und turbulente Reibung. *Z. Angew. Math. Mech, 1*, 233−252.

Wen, C.-Y., & Lin, C.-Y. (2001). Two-dimensional vortex shedding of a circular cylinder. *Phys. Fluids, 13*, 557−560.

Supplemental Reading

Friedrichs, K. O. (1955). Asymptotic phenomena in mathematical physics. *Bull. Am. Math. Soc., 61*, 485–504.

Lagerstrom, P. A., & Casten, R. G. (1972). Basic concepts underlying singular perturbation techniques. *SIAM Review, 14*, 63–120.

Meksyn, D. (1961). *New Methods in Laminar Boundary Layer Theory*. New York: Pergamon Press.

Panton, R. L. (2005). *Incompressible Flow* (3rd ed.). New York: Wiley.

Sherman, F. S. (1990). *Viscous Flow*. New York: McGraw-Hill.

White, F. M. (2006). *Viscous Fluid Flow*. New York: McGraw-Hill.

Yih, C. S. (1977). *Fluid Mechanics: A Concise Introduction to the Theory*. Ann Arbor, MI: West River Press.